

Dynamics of a 3-dimensional, baroclinic, headland eddy

Kerry Black , John Oldman & Terry Hume

To cite this article: Kerry Black , John Oldman & Terry Hume (2005) Dynamics of a 3-dimensional, baroclinic, headland eddy, New Zealand Journal of Marine and Freshwater Research, 39:1, 91-120, DOI: [10.1080/00288330.2005.9517294](https://doi.org/10.1080/00288330.2005.9517294)

To link to this article: <http://dx.doi.org/10.1080/00288330.2005.9517294>



Published online: 30 Mar 2010.



[Submit your article to this journal](#) 



Article views: 100



[View related articles](#) 



Citing articles: 7 [View citing articles](#) 

Dynamics of a 3-dimensional, baroclinic, headland eddy

KERRY BLACK

ASR Limited Marine Consulting and Research
P.O. Box 13048
Hamilton, New Zealand
email: k.black@asrltd.co.nz

JOHN OLDMAN

TERRY HUME

National Institute of Water and Atmospheric
Research Limited
P.O. Box 11115
Hamilton, New Zealand
email: j.oldman@niwa.co.nz and
t.hume@niwa.co.nz

Abstract Wave, current, and temperature measurements from the north side of Cape Rodney, north-eastern New Zealand, over a 6-week field programme, reveal the detailed internal dynamics of a baroclinic eddy. The measurements include water levels, currents, and water temperatures through the water column and seabed descriptions. A detailed calibration of a 3-dimensional numerical model leads to further examination of the flow and density structure within the eddy, in plan and cross-section. The eddy stretches c. 5 km along the northern side of the headland and is of the order of 1.5–2.0 km wide. The eddy currents are strongest near the bed and against the coast. The eddy is characteristically complex and vertical eddies readily form in parts of the water column during different phases of the tide, although these internal eddies rarely penetrate through the full depth. The dynamics near the surface and near the bed are significantly different and the structure of the eddy is often partitioned vertically and is strongly affected by wind.

Keywords eddy dynamics; headland; baroclinic; numerical modelling; Cape Rodney; New Zealand

INTRODUCTION

Eddies play a vital role in the ocean because they induce cross-shelf advection, bring nutrients to the surface in their core and can act to trap effluent or larval food along irregular coastlines. The eddy signature is important for biological production, larval transport, circulation, and mixing of all water-borne materials and micro-sized living organisms. At coastal headlands, eddies can elevate nutrient-rich bottom water to the surface, potentially creating zones of high biological productivity.

Linked field and numerical investigations of the parameters governing recirculation around headlands, islands, and reefs (Black & Gay 1987; Black 1989; Signell & Geyer 1991; Middleton et al. 1993) have provided considerable insight into the processes which induce and modify the rotating motion observed in coastal eddies. Further studies by Klinck (1996) and Perenne et al. (1997) and recent numerical studies by Lee et al. (1999a,b) have treated aspects of eddies in canyons and coastal embayments.

However, the evolution of processes leading to the formation of a headland eddy remain to be fully resolved. The complexity of the coastline and bathymetry (Falconer et al. 1986; Falconer & Mardapitta-Hadjipandeli 1987; Pattiaratchi et al. 1987; Deleersnijder et al. 1992; Denniss et al. 1995; Furukawa & Wolanski 1998), bottom friction (Signell & Geyer 1991), unsteadiness of flow (Black & Gay 1987), tidal excursion and current direction (Geyer & Signell 1991; Denniss et al. 1995), and horizontal eddy viscosity (Black 1989) have all been reported to influence eddy growth, size, shape, and decay in different situations.

In dealing with natural eddies in reversing tidal flows, Black & Gay (1987) suggested that inertia of the flow (which “jets” the water beyond the tip of the headland), internal friction, and the generated vorticity leads to the formation of a wake in the lee

of the obstruction. In reversing tidal flows, with reversal of the regional pressure gradients driving the tidal circulation, flow accelerates in the wake when the free stream offshore is still decelerating, and an eddy evolves. The presence of the wake pre-conditions the response to the oscillating tidal pressure gradients by creating spatial phase differences in the velocity patterns, which ultimately lead to the formation of what was coined a "phase" eddy (Black & Gay 1987). The name simply reflects the fact that the eddies form as a result of the presence of velocity phase differences which lead to spatial differences in the timing of flow reversal.

Black (1994) notes that phase eddies predominate on Australia's Great Barrier Reef where the bluff-like obstruction of the shallow reefs, rising sharply from a 40–60 m deep continental shelf, is ideal for phase eddy formation. Similarly, estuarine investigators have long noted the occurrence of velocity phase differences between the flood jet and ebb channels which lead to the formation of eddies around the time of flow reversal (e.g., Black & Healy 1982).

There has been some debate in the literature about the mechanism forming the wake and we do not attempt to fully address this matter in this paper. Here, we consider the consequences of the presence of the wake. That is, the paper examines the dynamics around the headland, particularly when the eddy is present. Specifically, we consider eddies observed at Cape Rodney headland (north-eastern New Zealand). Converging currents ($>0.5 \text{ m s}^{-1}$) around the tip of Cape Rodney set up counter-rotating eddies on the two sides of the headland that form on successive half tidal cycles (Hume et al. 1997a, 2000). The eddies have the characteristics of phase eddies (Black & Gay 1987), which develop after peak flow in unsteady currents, with strengthening return currents in the eddy while the free stream decelerates. Relatively strong return flows occur along the shoreline in the eddy (order 0.2 m s^{-1}) and the feature is so strong and regular that Hume et al. (1997a) were able to find the signature of the eddy in the seabed sediment facies.

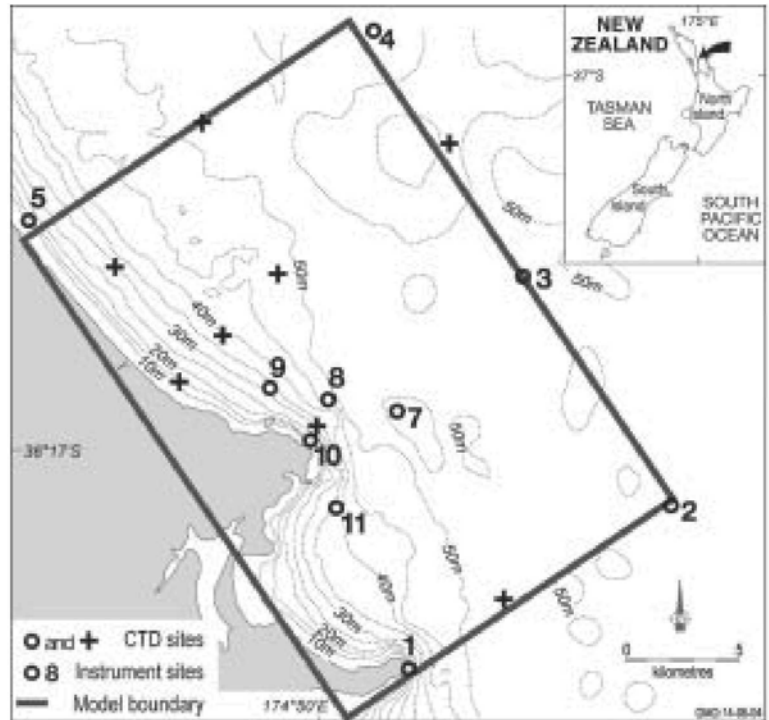
Research on wakes or eddies generated downstream of headlands has been primarily based on numerical models (Maddock & Pingree 1978; Pingree & Maddock 1979; Black & Gay 1987; Freeland 1990; Signell & Geyer 1991; Denniss & Middleton 1994). Galloway et al. (1996) compared four classical 3-dimensional models with observations from 26 current meters in the wake of Rattray Island. They found that all four models differed in

their ability to reproduce the islands' wake and all models underestimated the strength of the eddies behind the island. Previously, Black (1987) modelled the same Rattray Island data set to conclude that the explicit model used in the present paper (in its earlier 2-dimensional form) reproduced the size of the eddy more effectively than the implicit model adopted by Falconer et al. (1984), probably because of differences in numerical diffusion in the two models. It was concluded that the method to generate fast return flows in the numerical model is the application of high momentum diffusion (eddy viscosity) behind points of flow separation and low diffusion in the lee of the obstacle. This will normally generate numerical eddies which are as fast or faster than measured natural flows (Black 1989). Numerical tests showed that a 4–15 times increase in eddy strength could be induced by increasing eddy viscosity immediately behind the headland.

This means that eddy strength will be dependent on factors such as the abruptness of the headland and diffusion generating processes such as an irregular rocky reef, that may enhance eddy strength. The orientation and sharpness of the headland should further influence eddy character by affecting flow orientation in the jet, which is maintained by inertia. Similarly, the headland-seabed gradient will also influence eddy shape both horizontally and vertically. Further complication arises if the eddy is vertically-stratified by temperature or salinity. Given the expectation that the eddy will be strongly influenced by coastal morphology and circulation factors, such as tidal current strength and stratification, field measurements in a variety of morphologies and conditions are needed to further our understanding of these factors on eddy character. Furthermore, no field studies have to date recorded the effect of the stratification on phase eddy dynamics around a headland.

This paper presents a temporal data set of current, and temperature measurements made throughout and beyond a phase eddy on the north side of Cape Rodney over a 6-week field programme. With permanent thermistor strings, water levels, currents through the water column, and the seabed descriptions, a detailed calibration of the numerical model 3DD (Black 1995) is undertaken which expands the work by Black (1987) and Galloway et al. (1996) of validating model capacity. The model is then used to further examine the flow dynamics within the eddy. The complex dynamics of the eddy are depicted both horizontally and vertically. We find the signature of the eddy in the sea surface and

Fig. 1 Field location at Cape Rodney, New Zealand. Location of moored instruments (numbered sites as detailed in Table 1) and Conductivity-Temperature-Depth (CTD) casts (unnumbered sites). Model boundaries indicated by grey line.



cross-sectional temperature patterns and in the seabed characteristics and texture, as reported by Hume et al. (1997a, 2000). The phase of the recirculation relative to the free stream and the eddy shape are significantly altered by local morphology. The internal dynamics in the eddy are complex and cannot be viewed like a vortex in a stirred teacup (Wolanski et al. 1984, 1996).

Field location

Cape Rodney (36°17'S, 174°49'E) is a large coastal headland in the Hauraki Gulf, north-east New Zealand (Fig. 1). This triangular-shaped blunt-nosed feature protrudes 4 km into the Jellicoe Channel and into the main flow of waters entering the Hauraki Gulf. Moderate tidal flows of up to 0.5 m s^{-1} occur around the headland. Ocean swells arrive from the north to east sector. The headland separates extensive sand beaches of the Pakiri littoral cell in the north from sandy pocket beach and estuarine system in Omaha Bay to the south.

The headland is asymmetrical, has steep offshore topography, with the steepest isobaths and deepest water on the southern side. The northern side is mostly sandy seabed which, off the headland, grades to 30 m depth over c. 800 m cross-shore (1:26) and then to 45 m depth over an additional 1000 m (1:67).

Field programme

Measurements around the headland over 6 weeks from 3 February to 11 March 1997 recorded water level, currents, and temperatures through the water column (Fig. 1; Table 1).

Tides were measured at the four corners of the planned numerical model grid at sites 1, 2, 4, and 5, but sensor 5 failed. Currents in the vicinity of the eddy were measured using two Aanderaa current meters at site 7 (0.5 m and 22 m above the bed), bottom-mounted InterOcean S4 current meters at sites 8 and 11, and upward-looking Sontek Acoustic Doppler Profilers (ADPs) at site 9 and 10. The ADPs had a vertical bin resolution of 1 m. All instruments were programmed to record vector-averaged currents every 10 min.

With very little fresh water input to the region, the density stratification in the eddy is temperature related and a result of atmospheric heat inputs. Thus, permanent thermistor strings were deployed at all numbered sites at various depths (Fig. 1; Table 1). Temperatures were measured every 10 min using either a TidBit or WaDar thermistor. In addition, five surveys were conducted to measure the temperature field in more detail by recording vertical profiles with an Applied Microsystems

Conductivity-Temperature-Depth (CTD) instrument at all the sites around the headland (Fig. 1). CTD surveys were carried out on 17 and 24 February, 3 and 10 March, and immediately following retrieval of the instruments (15 March). All temperature measuring instruments were calibrated before and following use.

Previous investigations of circulation in the Hauraki Gulf (Black et al. 2000) have used the winds recorded in open water at the entrance of the Gulf on the low-lying Mokohinau Islands, located c. 50 km north-east of the headland. These were also adopted here for their relevance to overall Gulf circulation that influences the Cape Rodney dynamics through the measured water levels. The headland is sheltered by steep topography from the south-west quadrant (Fig. 1) and so local winds from this direction will be overestimated by the Mokohinau measurements in these conditions. Wind velocities (W) were converted for modelling purposes to an equivalent 10 m reading W_{10} in oceanographic convention (i.e., "blowing to") assuming the empirical altitude relationship:

$$\frac{W}{W_{10}} = \left(\frac{z}{10}\right)^k \quad (1)$$

where z = anemometer height (m) and k varies with atmospheric stability with a typical value of 1/7 (Beer 1997).

During the field programme, winds (Fig. 2) were variable and fortunately provided a broad range of conditions to study the eddy. Wind strengths reached between 16 and 23 m s⁻¹ on two occasions and varied c. 5–10 m s⁻¹ for much of the time. Calm periods occurred around Julian days 45, 50, 53–55, and 60.

Virtually all directions were well represented, although east to south-east winds predominated (Fig. 2).

Although the size of the field data set precludes full presentation in this paper, the data remains sparse in relation to the complexity of the eddy and so we use the numerical model in conjunction with the data to describe the eddy characteristics.

NUMERICAL MODELLING

The 3-dimensional baroclinic form of model 3DD is based on well-known momentum and mass conservation equations. An explicit finite difference (Eulerian) solution is used to solve the momentum and continuity equations for velocity and sea level, through a series of vertical layers that are hydrodynamically linked by the vertical eddy viscosity. The model provides for spatial variation in roughness length (z_0) and horizontal eddy viscosity (A_H). Non-linear terms and Coriolis force can be included or neglected, whereas the land/sea boundaries can be set to free slip or no-slip.

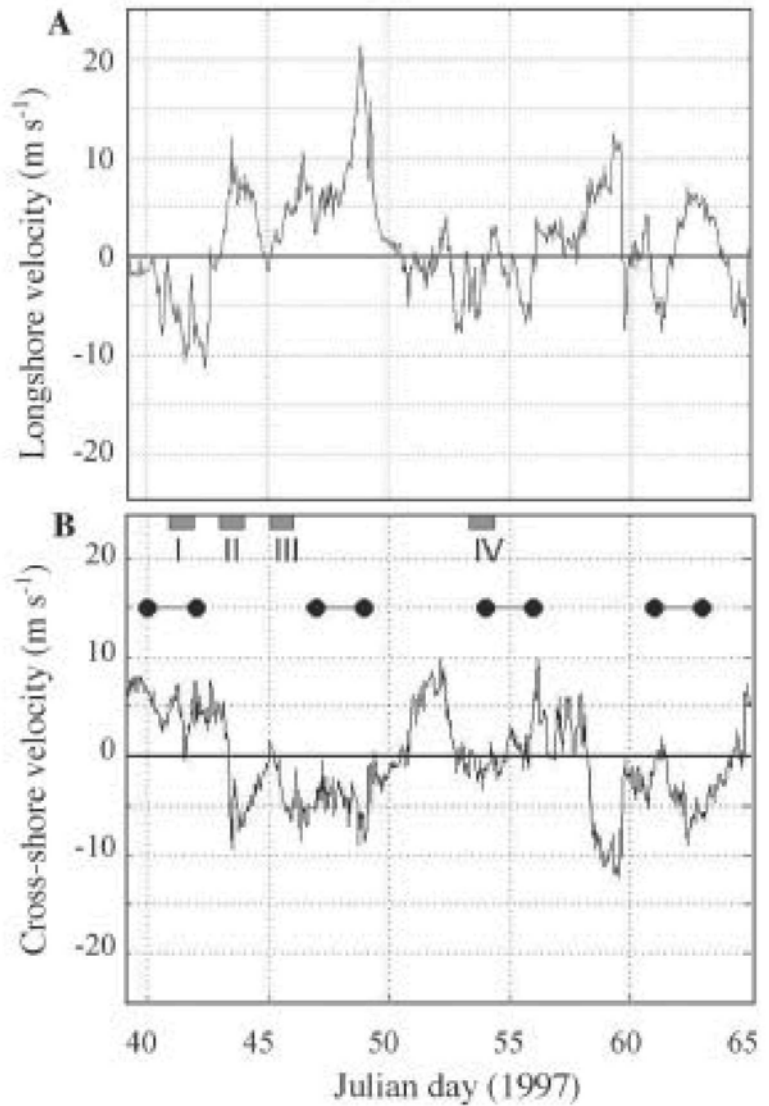
The model 3DD has been successfully applied and verified in a diverse range of situations (Black 1987, 1989; Black & Gay 1991; Black et al. 1993; Middleton & Black 1994; Young et al. 1994). The model has been previously applied to investigate the parameters responsible for eddy formation behind islands and reefs (Black & Gay 1987; Black 1989; Hume et al. 2000). The equations of horizontal motion for an incompressible fluid on a rotating earth in Cartesian coordinates with the z axis positive upward are:

Table 1 Details of each of the moorings strings given instrument type and depths.

| Site ID | Water depth (m) | Thermistors depths (m above bed)* | Instrument description |
|---------|-----------------|-----------------------------------|------------------------------------|
| 1 | 12 | 0.4 | InterOcean S4DW 0.5 m above bed |
| 2 | 50 | 16, 33, and 40 | OceanSoft SACM-3 0.5 m above bed |
| 3 | 50 | 2, 38, and 42 | Aanderaa WLR5 0.5 m above bed |
| 4 | 60 | 20, 40, and 50 | Aanderaa WLR7 0.5 m above bed |
| 5 | 14 | 0.6 | InterOcean S4A 0.5 m above bed |
| 7 | 56 | 38 and 45 | Aanderaa RCM4's 0.5 m above bed |
| 7 | 56 | | Aanderaa RCM4's 22 m above bed |
| 8 | 49 | 2, 16, 42, and 45 | InterOcean S4 33.9 m above bed |
| 9 | 35 | 0.6, 15, 25, and 31 | SonTek 500kHz ADP 0.5 m above bed |
| 10 | 25 | 0.6, 7, 13, and 22 | SonTek 1500kHz ADP 0.5 m above bed |
| 11 | 35 | 15 | InterOcean S4 13.6 m above bed |

*All sites had surface mounted thermistors.

Fig. 2 **A**, Cross-shore and **B**, longshore winds for the period of the field experiment. Julian day numbers reference to 0000 hours. Calibration periods (I–IV) are marked with a horizontal bar and periods during which the Conductivity-Temperature-Depth casts were made are marked by the dash/dot symbol.



$$\frac{\partial u}{\partial t} + u \frac{\partial u}{\partial x} + v \frac{\partial u}{\partial y} + w \frac{\partial u}{\partial z} - fv = -g \frac{\partial \zeta}{\partial x} - \frac{1}{\rho} \frac{\partial P}{\partial x} + A_H \left(\frac{\partial^2 u}{\partial x^2} + \frac{\partial^2 u}{\partial y^2} \right) + \frac{\partial}{\partial z} \left(N_z \frac{\partial u}{\partial z} \right) \quad (2)$$

$$\frac{\partial v}{\partial t} + u \frac{\partial v}{\partial x} + v \frac{\partial v}{\partial y} + w \frac{\partial v}{\partial z} + fu = -g \frac{\partial \zeta}{\partial y} - \frac{1}{\rho} \frac{\partial P}{\partial y} + A_H \left(\frac{\partial^2 v}{\partial x^2} + \frac{\partial^2 v}{\partial y^2} \right) + \frac{\partial}{\partial z} \left(N_z \frac{\partial v}{\partial z} \right) \quad (3)$$

$$w = -\frac{\partial}{\partial x} \int_{-h}^z u \, dz - \frac{\partial}{\partial y} \int_{-h}^z v \, dz \quad (4)$$

t is the time, u , v are horizontal velocities in the x , y directions respectively, w the vertical velocity (positive upward), h the depth, g the gravitational acceleration, ζ the sea level above a horizontal datum, f the Coriolis parameter, P the pressure, A_H the horizontal eddy viscosity coefficient, and N_z the vertical eddy viscosity coefficient, and ρ the density which varies with depth.

Assuming that vertical acceleration is neglected, the hydrostatic equation for the pressure at depth z is:

$$P = P_{atm} + \int_z^s \rho g dz \tag{5}$$

where P_{atm} is the atmospheric pressure.

The physical representations of each of the various terms in the momentum equation are: local acceleration; inertia; Coriolis; pressure gradient resulting from sea level variation; pressure gradient resulting from atmospheric pressure; horizontal eddy viscosity, wind stress, and bed friction. A_H varies spatially but the gradients are assumed to be small. Atmospheric pressure changes were not included in the simulations and therefore this term in the momentum equation is neglected.

The salt and heat balance component of the model is coupled to the hydrodynamics through the application of the baroclinic pressure gradient associated with the horizontal temperature and/or salinity density field. In the absence of evidence to the contrary, salinity was assumed to be constant and so only the temperature structure was modelled. The advection/diffusion equations are solved on the same grid as the hydrodynamics using a second-order-accurate, explicit, finite difference solution. The conservation equations for temperature may be written as:

$$\frac{\partial T}{\partial t} + u \frac{\partial T}{\partial x} + v \frac{\partial T}{\partial y} + w \frac{\partial T}{\partial z} = \frac{\partial}{\partial z} \left(K_z \frac{\partial T}{\partial z} \right) + K_H \left(\frac{\partial^2 T}{\partial x^2} + \frac{\partial^2 T}{\partial y^2} \right) \tag{6}$$

where T is temperature, and K_H, K_z are the horizontal and vertical coefficients of eddy diffusivity.

The density is computed according to an equation of state of the form:

$$\rho = \rho(T, S, z) \tag{7}$$

with salinity of 35 ppt. The boundary conditions at the free surface $z = \zeta$ are:

$$N_z \frac{\partial u}{\partial z} = \tau_x^s \quad N_z \frac{\partial v}{\partial z} = \tau_y^s \quad \frac{\partial \zeta}{\partial t} + u \frac{\partial \zeta}{\partial x} + v \frac{\partial \zeta}{\partial y} = w^s \tag{8}$$

where τ_x^s, τ_y^s denotes the components of wind stress, w^s is the vertical velocity at the surface, and

$$\tau_x^s = \rho_a \gamma |W| \frac{W_x}{\rho} \quad \tau_y^s = \rho_a \gamma |W| \frac{W_y}{\rho} \tag{9}$$

ρ is the water density, W the wind speed at 10 m above sea level while W_x and W_y are the x and y components, γ is the wind drag coefficient, ρ_a the density of air.

The wind drag coefficient comes from the work of Wu (1982) where the drag coefficient γ is of the form:

$$\gamma = (0.8 + 0.065 W_s) \times 10^{-3} \tag{10}$$

where W_s is the numerical value in $m s^{-1}$ of the wind speed at 10 m above sea level.

Surface boundary conditions for salinity and temperature were not required, as there was assumed to be no flux through the surface at the time-scales modelled.

Assuming seabed slope is small, at the seabed, $z = -h$, we have:

$$N_z \frac{\partial u}{\partial z} = \tau_x^h \quad N_z \frac{\partial v}{\partial z} = \tau_y^h \tag{11}$$

where τ_x^h, τ_y^h denotes the components of bottom stress. Applying a quadratic law at the seabed:

$$\tau_x^h = g u_h \left(u_h^2 + v_h^2 \right)^{1/2} / C^2$$

$$\tau_y^h = g v_h \left(u_h^2 + v_h^2 \right)^{1/2} / C^2 \tag{12}$$

with u_h, v_h being the bottom currents and C is Chezy's C . For a logarithmic profile:

$$C = 18 \log_{10}(0.37 h/z_0) \tag{13}$$

where z_0 is the roughness length.

The equation of state in a salinity-stratified condition can be approximated as:

$$\rho = \rho_0 + \alpha S \tag{14}$$

where α is 0.74 at 20°C and ρ_0 is the density of fresh water (1000 kg m^{-3}).

The equation of state in a temperature and salinity stratified condition can be approximated as:

$$\rho = 1000 (1.0 - 3.7 \times 10^{-6} T^2 + 8.13 \times 10^{-4} S) \tag{15}$$

where $T = T' + 2.7$ and T' is the temperature in °C, S is the salinity (taken as 35 ppt).

For the temperature-stratified simulations, the vertical eddy viscosity and diffusivity is based on a mixing length and Richardson number formulation, as:

$$l_m(z) = \kappa z' \left(1 - \frac{z'}{h} \right) \quad \text{and} \quad N_0(z) = l_m^2 \left[\left(\frac{\partial u}{\partial z} \right)^2 + \left(\frac{\partial v}{\partial z} \right)^2 \right]^{1/2} \tag{16}$$

where $N_0(z)$ is either the eddy viscosity N_z or eddy diffusivity K_z at elevation z' above the seabed, l_m is the mixing length, and κ is the Von Karman constant set to 0.4. In stratified flows, the gradient Richardson Number is:

Downloaded by [125.239.173.16] at 06:38 29 August 2017

$$R_i(z) = \left(\frac{g}{\rho} \left(\frac{\partial \rho}{\partial z} \right) / \left(\frac{\partial u}{\partial z} \right)^2 \right) \quad (17)$$

To determine the reduced vertical eddy viscosity and diffusivity in stratified flows, we use the Perrels & Karelse (1982) formula:

$$N(z) = N_0(z) e^{-\alpha R_i(z)} \quad (18a)$$

$$K(z) = K_0(z) e^{-\alpha R_i(z)} \quad (18b)$$

where $\alpha = 4$ and 12 for the eddy viscosity and eddy diffusivity respectively.

To solve the equations by the finite difference method, a staggered finite difference grid is utilised similar to that applied by Leendertse & Liu (1975). The sea level replaces w in the top layer. The solution is found by time stepping with a second-order-accurate explicit scheme and third-order approximations for the non-linear inertia terms.

A z -coordinate model is favoured over a sigma coordinate model to eliminate problems encountered when representing horizontal density gradient in a grid with non-horizontal grid cells. Similarly at the seabed, layered models typically represent a sloping seabed by a series of steps, with heights equal to the model's vertical grid size. In baroclinic simulations, this can create local upwelling at the step walls, which is an artifact of the model's vertical resolution. These local upwellings can penetrate through the water column, causing a pattern of false internal wave activity. In 3DD, the depth is reproduced accurately by allowing fractionated cell sizes at the bed, which are less than the vertical grid size. The merits of the scheme have been assessed by simulating the steep profile used by Lamb (1994) which is a challenging test of the model.

Figures 3A and 3B respectively show the isopleths of density without and with fractionated cell sizes. Figure 3A shows that the grid-thickness steps in the bathymetry lead to unwanted oscillations in the isopleths at the crest of the steeply rising bathymetry. Closer inspection shows that the crest of each oscillation is associated with upwelling on the face of each step. The oscillations are not occurring with the fractionated depth scheme (Fig. 3B) and the velocities on the steeply-rising "continental shelf" vary smoothly in the model. Further confirmation of the importance of this scheme is shown in Fig. 3C, where sharp variations in the isopleths on steep slopes are reproduced without instability.

For the model simulations at Cape Rodney, salinity was assumed to be vertically uniform in

accordance with observations. To model the temperature structure, a centred explicit finite difference scheme was used, similar to that used for the hydrodynamics. Other aspects of the model of relevance to the Cape Rodney region are described by Black et al. (2000) who consider the 3-dimensional baroclinic circulation of the surrounding Hauraki Gulf.

Bathymetry

For the model bathymetry, a 400 by 400 m grid was constructed from the Royal New Zealand Navy fair sheets (relative to Chart Datum). Gridding of the raw bathymetry data was carried out using Kriging in SURFER™. The cell size was chosen to resolve important features of the flow identified by earlier field measurements (Hume et al. 1997a). Similarly, to resolve the vertical structure of the eddy the resolution in the vertical was set to 4.5 m giving a total of 15 layers within the model.

Model boundary conditions

Hydrodynamic forcing in all simulations occurs at the southern, eastern, and northern model boundaries, placed at a sufficient distance so as not to directly impinge on the eddies (Fig. 1). Along the southern and eastern boundaries where tide gauges were functioning on each corner of the model grid, the water levels from the bounding sensors were linearly interpolated onto the boundary cells. As the region is small, there was no need to extract further information from regional models (Black et al. 2000). At the northern boundary, the loss of water level data from the instrument which failed at the shoreward end of the boundary was overcome by redeploying an instrument at the same site for an additional 6 weeks, undertaking tidal analyses, and reconstituting a sea level record. The low frequency (non-tidal) component was taken from the offshore gauge at site 4 and added to the reconstituted tidal levels, thereby accounting for all measured oscillations.

Although 3DD has the capacity to simulate atmospheric heat transfers and the evolution of the thermocline, we felt this form of calibration was well beyond the limits of the present paper. As such, for the fully temperature-stratified modelling, it was necessary to establish an initial temperature distribution in the model at the cold start and only relatively short duration baroclinic simulations (2 days) were made in the absence of incorporating ocean-atmosphere heat inputs and losses.

Four different periods were chosen for detailed simulations and the initial distribution of temperature

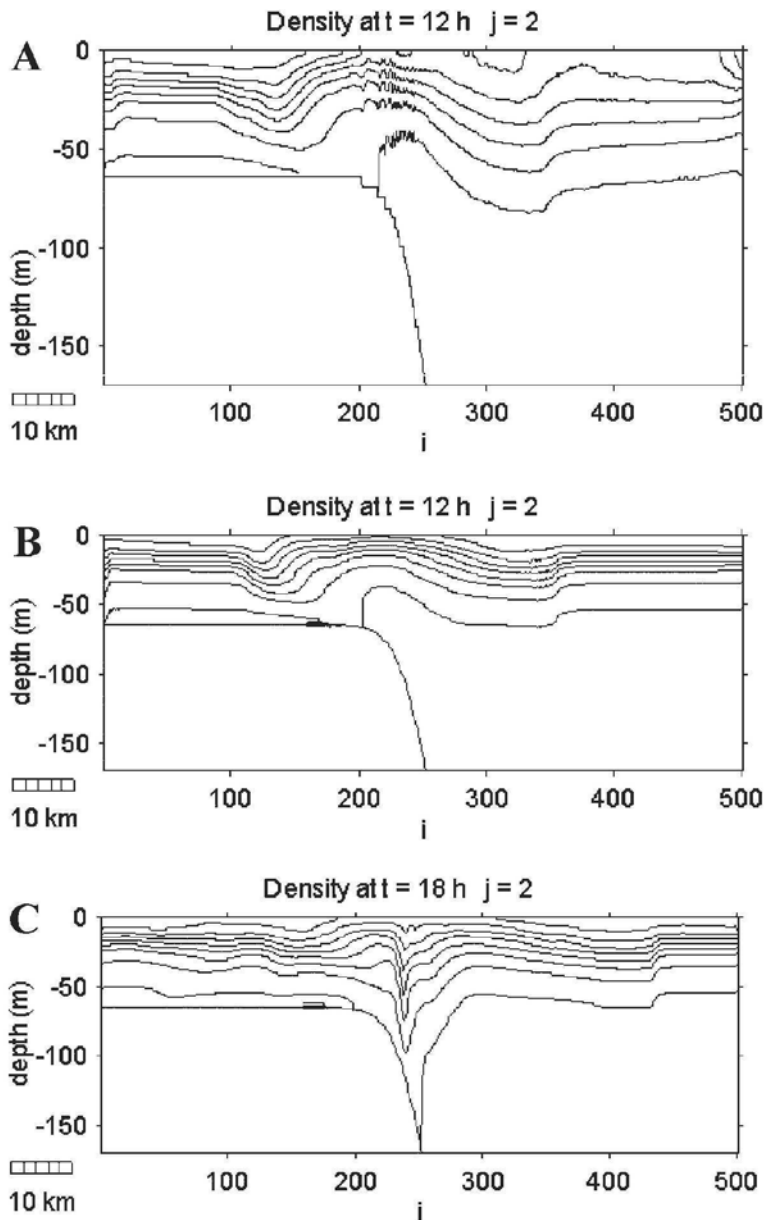


Fig. 3 A, Isopleths at 12 h with flow across a steeply-sloping continental shelf, using the bathymetry adopted by Lamb (1994). In this example, the bathymetry in Model 3DD is represented as a series of steps, without fractionated layers, and instabilities in the contours are evident at the crest of the slope. B, Isopleths at 12 h with flow across a steeply-sloping continental shelf, using the bathymetry adopted by Lamb (1994). In this example, Model 3DD adopts fractionated seabed layers and no instabilities are evident in the contours at the crest of the slope. C, Isopleths at 18 h with flow across a steeply-sloping continental shelf, using the bathymetry adopted by Lamb (1994). In this example, Model 3DD adopts fractionated seabed layers. The model is predicting sharply-varying isopleths at the crest of the slope.

for each of these was interpolated onto the model grid using the high-frequency measurements from the thermistor strings as follows. The thermistor data were first averaged over the 50 h before to the start of the simulation. This time span was chosen because it represents a sufficiently long period to represent the average conditions, and eliminate short-term fluctuations in temperature. The time equates to 4 tidal cycles (with the M_2 dominating at the site) thereby eliminating tidal cycle aliasing.

Data from the thermistor strings showed that below 40 m there was generally very little temperature variation. Therefore, for sites where the thermistor strings did not extend to the very bottom of the water column the deepest measured temperature was extended to the seabed. The data were then interpolated vertically at the centre of each model layer. With the close spacing of the sensors in relation to the gradients in the thermocline, it was found that linear interpolation was adequate. A horizontal interpolation of the

temperatures was then undertaken throughout each layer. A linear interpolation was used after finding that more sophisticated techniques, like Kriging interpolation, created obviously false horizontal oscillations in the temperatures.

The correctness of the boundary techniques is confirmed by the model calibration below. In the next sections of the paper, we describe the 2-dimensional circulation and field measurements and undertake calibration of the baroclinic model. This then leads to application of the model, supporting the measurements, to depict the eddy dynamics. Notably, the temperature stratification acts as an easily-visualised “tracer” of the movement of water in the eddy and so temperature pattern evolution is presented for that purpose, and stratification is also shown to influence eddy dynamics.

2-dimensional circulation patterns

The measured tides at Cape Rodney are predominantly M_2 (lunar semi-diurnal) of 1.8 m amplitude with a spring-neap amplitude modulation created by the solar semi-diurnal S_2 (second largest) constituent (0.3 m). As such, the dominant tidal cycle duration is 12.42 h.

The 2-dimensional circulation patterns about the headland, generated numerically by Hume et al. (1997a), are reproduced in Fig. 4. Initially at slack high water in the free stream, strong flows have already developed on the south side and about the headland (Fig. 4A). Two hours after high water, a wake develops to the north in the lee of the headland (Fig. 4B). At 4 h after high water (i.e., 1 h after peak flow), the currents in the wake begin to accelerate towards the headland while the free stream continues to decelerate (Fig. 4C). Six hours after high water (around slack low tide) the currents along the headland are strong, the free stream is essentially stationary (Fig. 4D), and the core of the eddy has migrated towards the tip of the headland. The same pattern evolves on the south side of the headland in the next 4 h (Fig. 4E,F).

The dominant dynamical features are: (1) the convergence of flow on the headland (Fig. 4A); (2) a wake in the lee of the headland (Fig. 4B); (3) continuation of a jet-like flow adjacent to the wake from the headland tip and the formation of the eddy (Fig. 4C); (4) strong return flow when the free stream currents are slack; and (5) south-east migration of the eddy core (Fig. 4D). The eddy has the classic features of a phase eddy (Black & Gay 1987).

In the following sections, detailed temperature, current, and sea level measurements within and

about the eddy show the 3-dimensional dynamics of the eddy, and are used to establish and test a baroclinic hydrodynamic and advection/dispersion model. The current meter measurements were made on the northern side of the headland and so the southern eddy is not considered in much detail here, although a comparison of the two eddies with their different underlying seabed gradients would be informative.

Temperature time series

Features of the water column temperature time series (measured by the thermistors) are well depicted by Fig. 5 (A–D) which presents near-surface (0.5 m) and mid-depth (12.5 m) temperatures at four sites. The chosen sites are site 5 which is beyond the eddy at the coast, site 7 in deep water off the headland in the free stream, site 10 adjacent to the headland in the eddy return flow, and site 9 further offshore near the core of the eddy (Fig. 1). The air temperature and solar radiation are shown with the water temperature time series (Fig. 5E,F).

In general, the overall patterns are similar, but some pronounced differences occur. A tendency for temperature to increase then decrease over the 34 recording days is common. Major peaks are evident throughout, particularly around days 55 and 63 during periods of rising solar radiation when the water becomes highly stratified by 2–3°C between the bed and the surface at site 5 (Fig. 5A). All sites exhibit a diurnal oscillation, and a superimposed semi-diurnal cycle also occurs (e.g., site 7 from days 60–65, Fig. 5B). Vertical temperature differences are small during the cooling events, as expected (e.g., from days 46–50, 57–60, and 68–70), whereas the loss of stratification around day 68 relates to a reduction in air temperature and freshening winds (Fig. 2), before the reduction in solar radiation at day 70. The thermocline is broken down during periods of cooling air temperature and rising onshore (south-east quadrant) winds.

The differences between the four sites are significant. Close to the coast beyond the eddy at site 5 (Fig. 5A), the duration of the strongly-stratified periods is longer than at the other sites. For example, a strong vertical temperature gradient is established around days 53 and 62 and retained for 3–4 days. Although the figure is not shown, no similar pattern is observed at the other sites suggesting different dynamics (advection and mixing) around the headland than along the open-coast beach at site 5. One obvious difference to explain this result, shown by the numerical

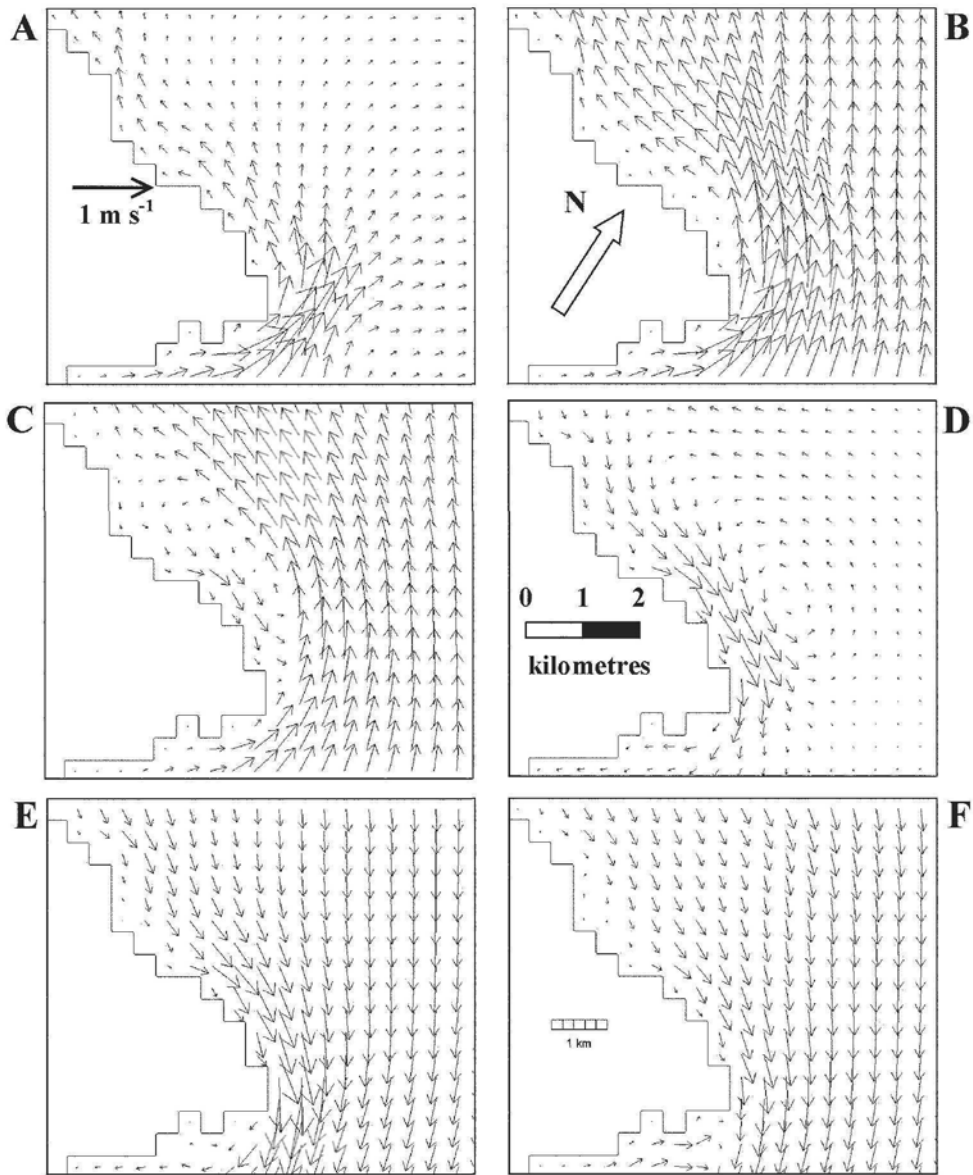


Fig. 4 Depth-averaged velocity vectors from the 2-dimensional model of Hume et al. (1997) at: **A**, high water; **B**, high water + 2 h; **C**, high water + 4 h; **D**, high water + 6 h (around low water); **E**, high water + 8 h; and **F**, high water + 10 h. Arrow tails are scaled on velocity with scale shown in A. Model grid is rotated and north direction is shown in B.

modelling in Fig. 4, is the slower tidal currents at site 5.

The most striking difference between the sites occurs along the shoreward side of the eddy and close to the tip of the headland at site 10 (Fig. 5C). Here thermal gradients are smaller and a much stronger temperature oscillation is evident at 12.5 m.

The diurnal frequency is linked to the diurnal solar radiation pattern, but the magnitude of the oscillation indicates larger vertical movement of the thermocline than elsewhere. Thus, we infer that the strongest vertical currents may occur against the coast in the eddy return flow along the north side of the headland (Fig. 4D), and this is reconsidered later.

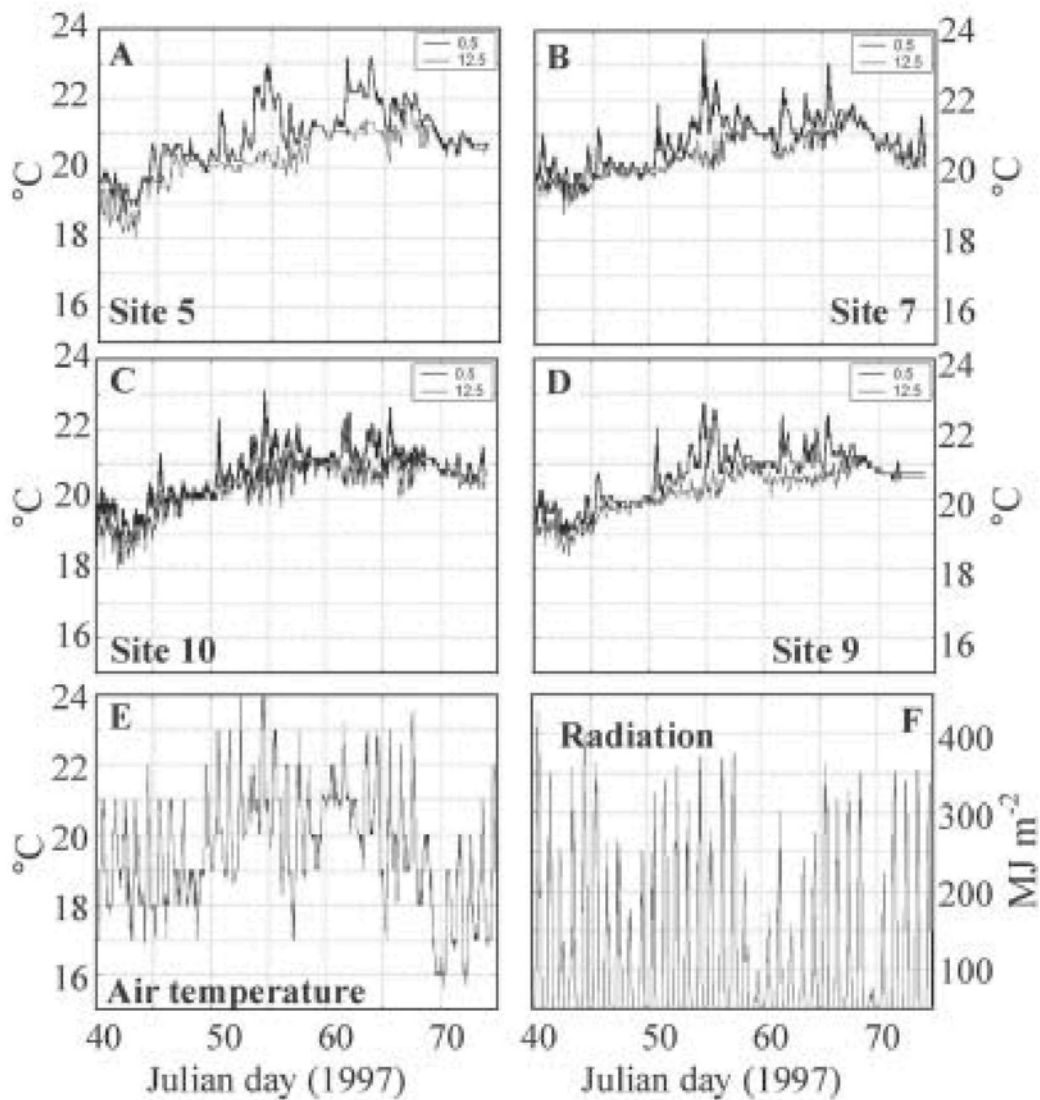


Fig. 5 Temperature time series from 0.5 m below the surface (darker line) and at 12.5 m (lighter line) below the surface for: **A**, site 5; **B**, site 7; **C**, site 10; and **D**, site 9. **E**, Air temperature; and **F**, solar radiation.

HYDRODYNAMICS AND MODEL CALIBRATION

Homogeneous model simulations for calibration

The complete 35-day period of measurements was simulated with the homogeneous 3-dimensional model. The highest correlation between the model and measured time series at sites 7 and 8 for the full 35-day period (r^2 of 0.87 and 0.73 respectively) was

achieved with the seabed roughness length set to $z_0 = 0.007$ m and the horizontal eddy viscosity coefficient set to $A_H = 5 \text{ m}^2 \text{ s}^{-1}$. All other parameters such as the vertical eddy viscosity and the wind drag coefficient are calculated by the model (Equations 18, 17, and 10 respectively) and therefore are not calibration parameters. To validate the model, baroclinic simulations were carried out for the four calibration periods referred to in Fig. 2 (see results later).

3-dimensional baroclinic circulation for validation

Near-bed (3.7 m above the bed) and near-surface (31.7 and 21.7 m above the bed respectively) flows at sites 9 and 10 from the ADP are shown for the four calibration periods (Fig. 6 and 7 respectively). The concurrent winds are presented in Fig. 2 and the conditions during these times are summarised in Table 2.

The current patterns at both sites exhibit unusually complex behaviour. At the more offshore site 9, subsurface currents are in phase with but much faster than the near-bed flows at times (Fig. 6A). Mostly the subsurface is faster than the bed, but around day 54 the bed flows are faster (Fig. 6D). At times, the subsurface consistently lags by c. 2 h with large differences between surface and near-bed current magnitudes (Fig. 6C). At other times, the magnitudes are similar, even though the lag remains (Fig. 6E). Subsurface flows are nearly always strongly ebb dominant, implying positioning within the jet off the headland. Near-bed flows are more neutral. Cross-shore currents are relatively small and, typically, the bed and surface are sometimes up to 180° phase lagged, but periods of synchronous flow also occur (Fig. 6B,D,F,H). We speculate that the cause of the variation relates to flow acceleration.

There are substantial differences between sites 9 and 10, as expected given their positions relative to the headland and the fact that site 9 is over 30 m depth and site 10 is less than 10 m depth. The phase lags in longshore currents between the surface and bed are no longer apparent (Fig. 7). During the first period (Fig. 6A, 7A), site 9 shows strong flows to the north at the subsurface whereas site 10 shows strong flows to the south. Similarly, the strengthening of the near-bed flow and weakening of the subsurface flow after day 44.5 at site 9 is opposite at site 10 where the flood flows are very weak (Fig. 6E, 7E). This is interpreted as a shift in the eddy preventing site 10 from flooding, whereas the same shift in the velocity gradients in the jetting flow past the headland causes site 9 currents to increase.

Site 10 is strongly net flood when averaged over the tidal cycle, in accordance with its position within the return flow of the eddy. The duration of the return current phase is also longer at site 10 than site 9, as expected, but more pronounced at the surface. Cross-shore currents are relatively small and irregular, and often phase lagged by 180°. The lag happens during strong winds (Fig. 7B) and is much less pronounced in calm weather (Fig. 7C,D).

In summary, the eddy dynamics are characteristically complex and irregular within and between different tidal cycles. Eddy strength varies from cycle to cycle (e.g., Fig. 6G) and shear between the bed and surface is common, but also variable (Fig. 6E). Surface flows are considerably stronger, particularly during the ebb phase (Fig. 6A). Site 10 is mostly well within the eddy return flow as demonstrated by the flood dominance (Fig. 7A).

Sea-surface temperature observations

Although CTD surveys were recorded over several hours (usually 4 h) and cannot be considered as instantaneous, the signature of the eddy and other features in the surface layer have some resilience at this time-scale. Thus, we examine surface temperatures interpolated from the CTD surveys and the moored thermistor strings to: (1) seek trends, rather than instantaneous values; (2) look for surface manifestations of the eddy; and (3) examine the effect of wind on the surface layers (Fig. 8).

High variability in the sea surface temperatures is apparent throughout but evidence of the eddy appears in all four surveys. For example, the tongue of warmer water to the north of the eddy in Fig. 8A, the shape of the cold patch to the north of the eddy in Fig. 8B, the cold patch in the core of the eddy in Fig. 8C, and the double cold patch in Fig. 8D are all indicative of upwelling in the eddy.

The shape of the patch in Fig. 8B and the multiple cold patches in Fig. 8D are related to advection of the surface waters by headland tidal currents, as already demonstrated by Black et al. (2000) and

Table 2 Average wind conditions for the four selected calibration periods.

| Simulation | Start time (Julian day) | Average wind speed (m/s) | Average cross-shore wind speed (m/s) | Average longshore wind speed (m/s) |
|------------|----------------------------|--------------------------------|--|--|
| I | 10 Feb (40.9) | 8.7 | 2.8 | -7.4 |
| II | 12 Feb (43.0) | 9.7 | -6.0 | 7.4 |
| III | 15 Feb (45.0) | 6.9 | -5.3 | 4.3 |
| IV | 23 Feb (53.4) | 2.1 | -0.9 | 0.5 |

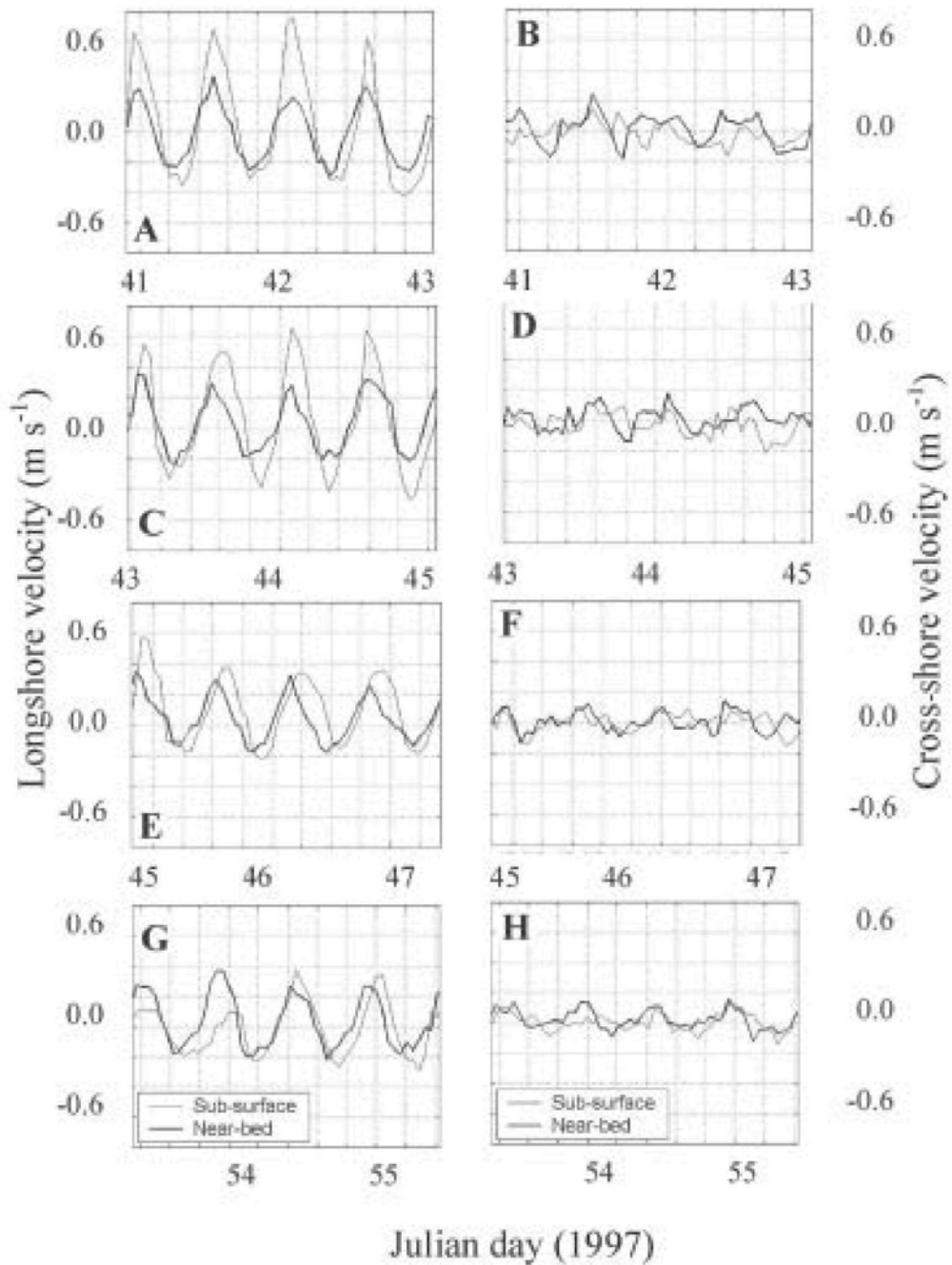


Fig. 6 Velocities 3.7 m above the bed (near-bed, dark line) and 31.7 m above the bed (near-surface, light line) from the Acoustic Doppler Profiler moored at site 9 during the four calibration periods. Left column shows longshore currents and the right column shows cross-shore currents.

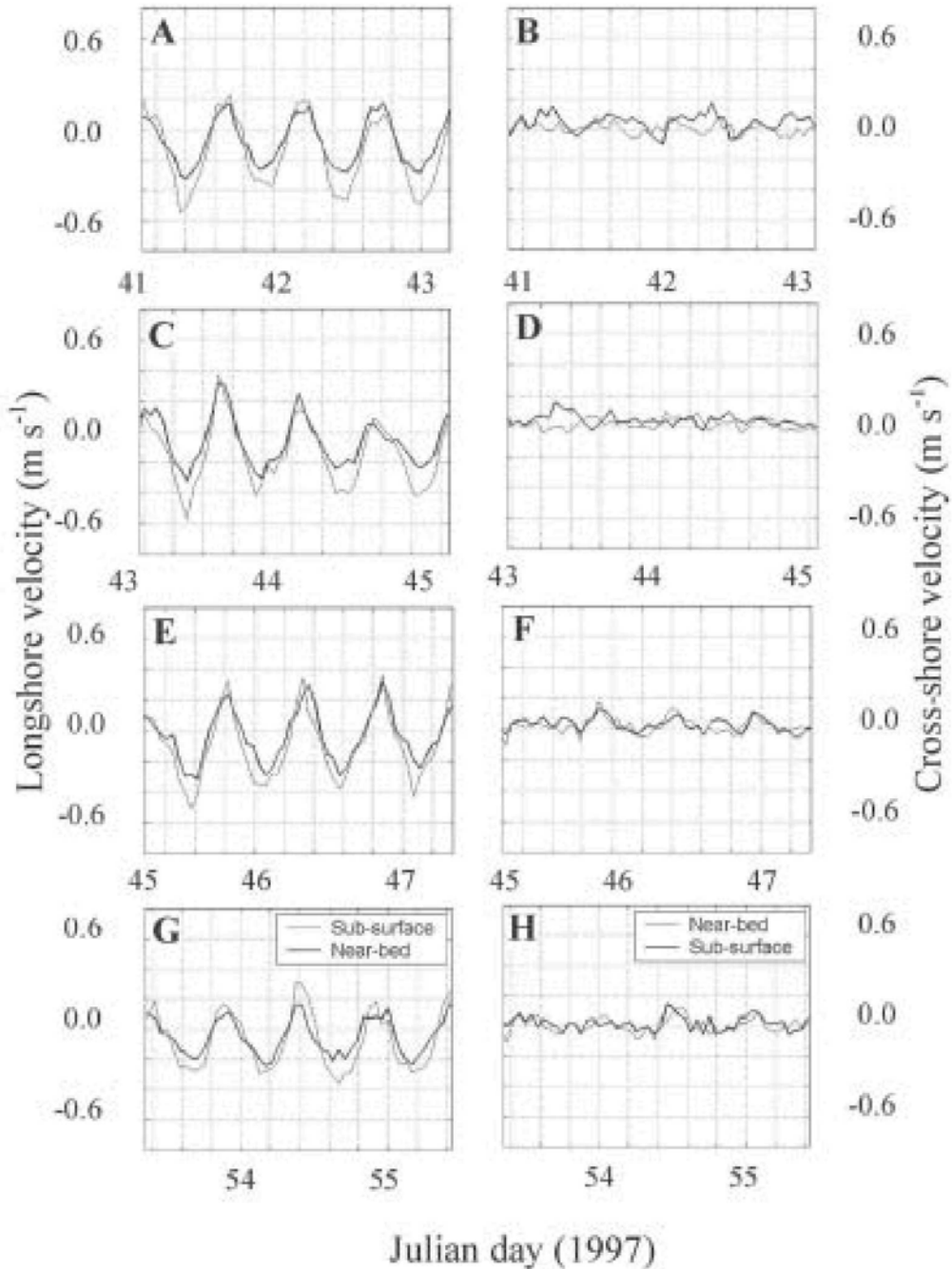


Fig. 7 Velocities 3.7 m above the bed (near-bed, dark line) and 21.7 m above the bed (near-surface, light line) from the Acoustic Doppler Profiler moored at site 10 during the four calibration periods. Left column shows longshore currents and the right column shows cross-shore currents.

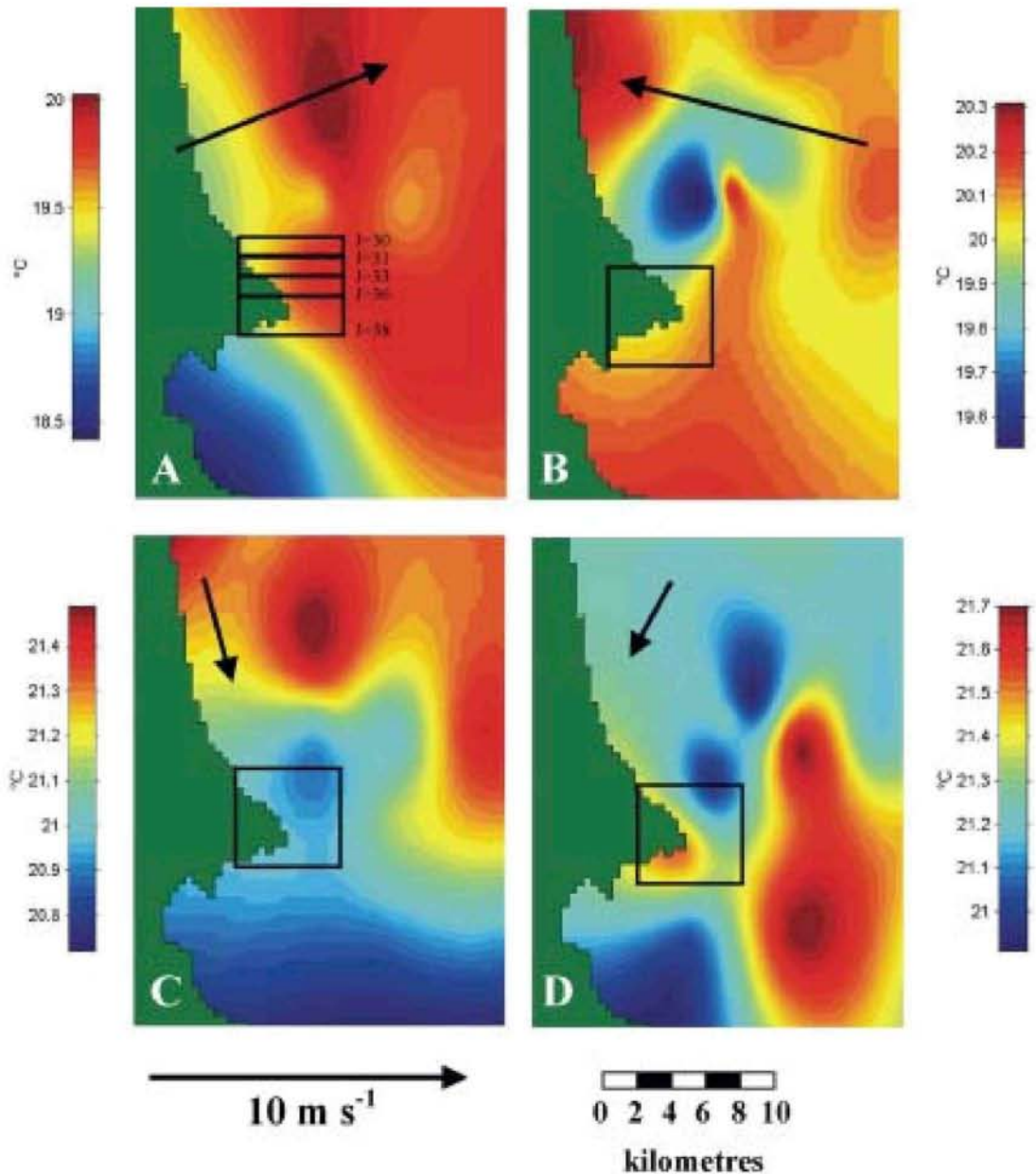


Fig. 8 Interpolated surface temperature data from Conductivity-Temperature-Depth (CTD) casts taken during: **A**, Julian day 47; **B**, Julian day 61; **C**, Julian day 54; and **D**, and Julian day 40. Lines in **A** show transects through model cells $J = 30, 31, 33, 36,$ and 38 , within the box defining the model sub-area used to examine eddy dynamics. Vectors show the average wind conditions in the 24 h before the start of the CTD survey.

shown later with the model. In all instances there is also a propensity for the formation of a relatively hot zone with integrated hot patches, forming in deeper water beyond the eddy.

The size of the cold patch north of the headland increases as the wind turns from the longshore (Fig. 8C) to cross-shore (Fig. 8D). The south-west wind (Fig. 8A) is upwelling favourable and characterised

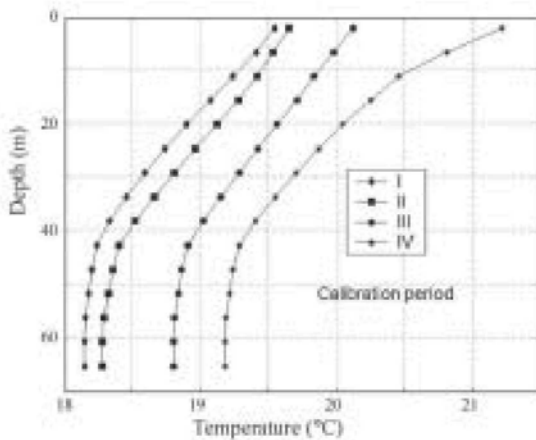


Fig. 9 Measured vertical temperature profiles for the four calibration periods. (I, Julian day 40.9; II, Julian day 43.0; III, Julian day 45.0; and IV, Julian day 53.4.)

by the classic pattern of cold water upwelling along the coast with a lower temperature overall and the broadest temperature range of over 1.5°C. The eddy is evidenced by a tongue of colder water oriented cross-shore that rotates to the south offshore. The pattern is similar to, but less pronounced than, the cold patch under south-easterlies in Fig. 8B.

A similar variation in upwelling under different wind conditions around Cape Rodney eddy was noted in satellite images of the headland by Black et al. (2000, fig. 11). The strongest upwelling occurred after north-west winds.

Baroclinic calibration

With the incorporation of temperature stratification, model velocity calibration was undertaken over the four periods considered in Fig. 7 and 8 and summarised in Table 2. The mean temperature profiles over the four calibration periods (50 h) from all thermistor sites (Fig. 1) are shown in Fig. 9. In general, the observed profile is nearly linear to c. 40 m, and relatively constant below 40 m.

Initial conditions for the temperature structure were interpolated values from the measurements, before each of the four periods modelled. The model was started at high tide, when flows are close to zero, and so an initial velocity field of zero current speed was adopted. The model was run for one tidal cycle to damp out any initial oscillations and recover from the “cold” start, before accepting any predictions.

Although all sites were examined, we present these two only (i.e., sites 9 and 10), for their sensitivity to eddy dynamics. From the homogeneous

simulations the match between the measured and modelled data are least accurate in the period from day 45 to 47 and so we present this period as the most stringent test of the model. The results at other times are similar and therefore not presented. Figures 10 and 11 present baroclinic model calibration examples at eddy sites 9 and 10 respectively. Time series are presented at 6, 18, and 24 m above the bed at site 9, and 2, 7, and 11 m above the bed at site 10. These depths correspond to the bottom, middle, and top bins of the ADP.

Additionally, the isotherm dynamics in cross-section through the eddy on the headland are considered for further confirmation of model behaviour (Fig. 12, 13). Here, the temperatures are interpolated from the thermistor strings through sites 10, 9, 8, 7, and 3 and compared to the model transect for $J = 33$ (Fig. 8A). Once again, a linear interpolation was used after finding that more sophisticated techniques (such as Kriging) created obviously false oscillations in the temperatures. Because there is very little temperature variation below 40 m, the deepest recorded temperature was duplicated through to the seabed to avoid extraneous extrapolation at depth. The sites used for the interpolation are not exactly on a straight line (Fig. 1) and the thermistor data are sparser than the model resolution. However, comparisons remain useful and informative. We show the temperatures at 3-hourly intervals over a tidal cycle at high tide, 3 h, low tide, and 9 h for the four examples. The positions of the thermistors in the interpolated cross-section are shown as black dots, and it is evident that the data are sparse in places, particularly below c. 18 m. Here, these examples are considered for model calibration, but subsequently they are used to describe eddy dynamics. Thus, the model output is retained to the coast, whereas the measured data start at site 10 in 25 m depth and much of the predicted vertical structure occurs very close to the coast beyond the range of the measurements. These figures also show the cross-shore current magnitudes in the cross-section, which are discussed later.

Baroclinic calibration results: currents

At site 9, the prediction of the current magnitudes can be seen to agree with the measurements (Fig. 10). The discrepancy between the model and observations is greatest in the first tidal cycle, because of the cold start. Phase prediction near the bed is good and the model partially reproduces the significant lag at peak positive flow, measured to be as much as 2.5 h between the bed and the surface (Fig. 10). Although

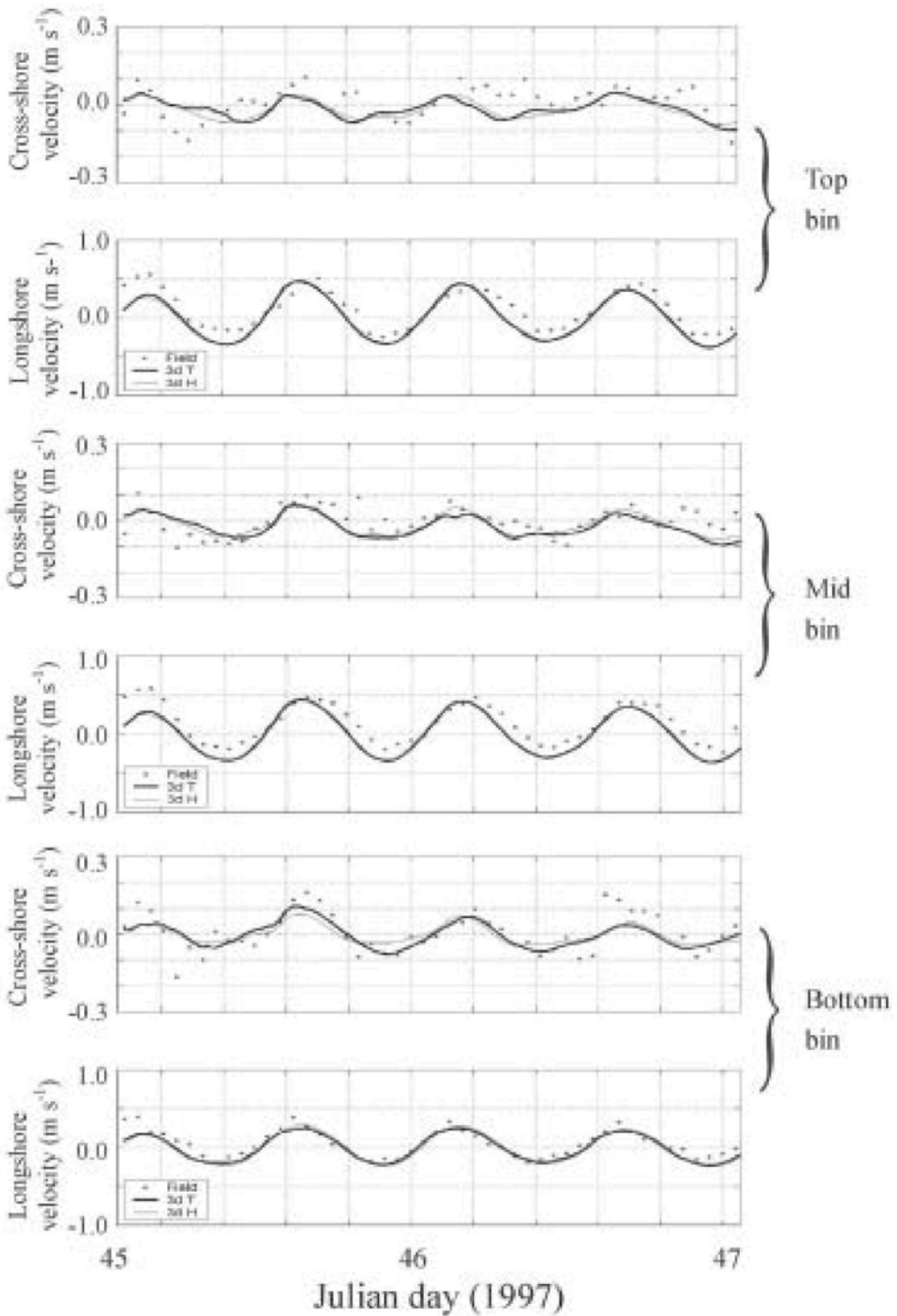


Fig. 10 Comparison of the calibrated barotropic (light solid line) and baroclinic (heavy solid line) model with measurements (dots) at site 9, for near-surface, mid-water, and near-bed.

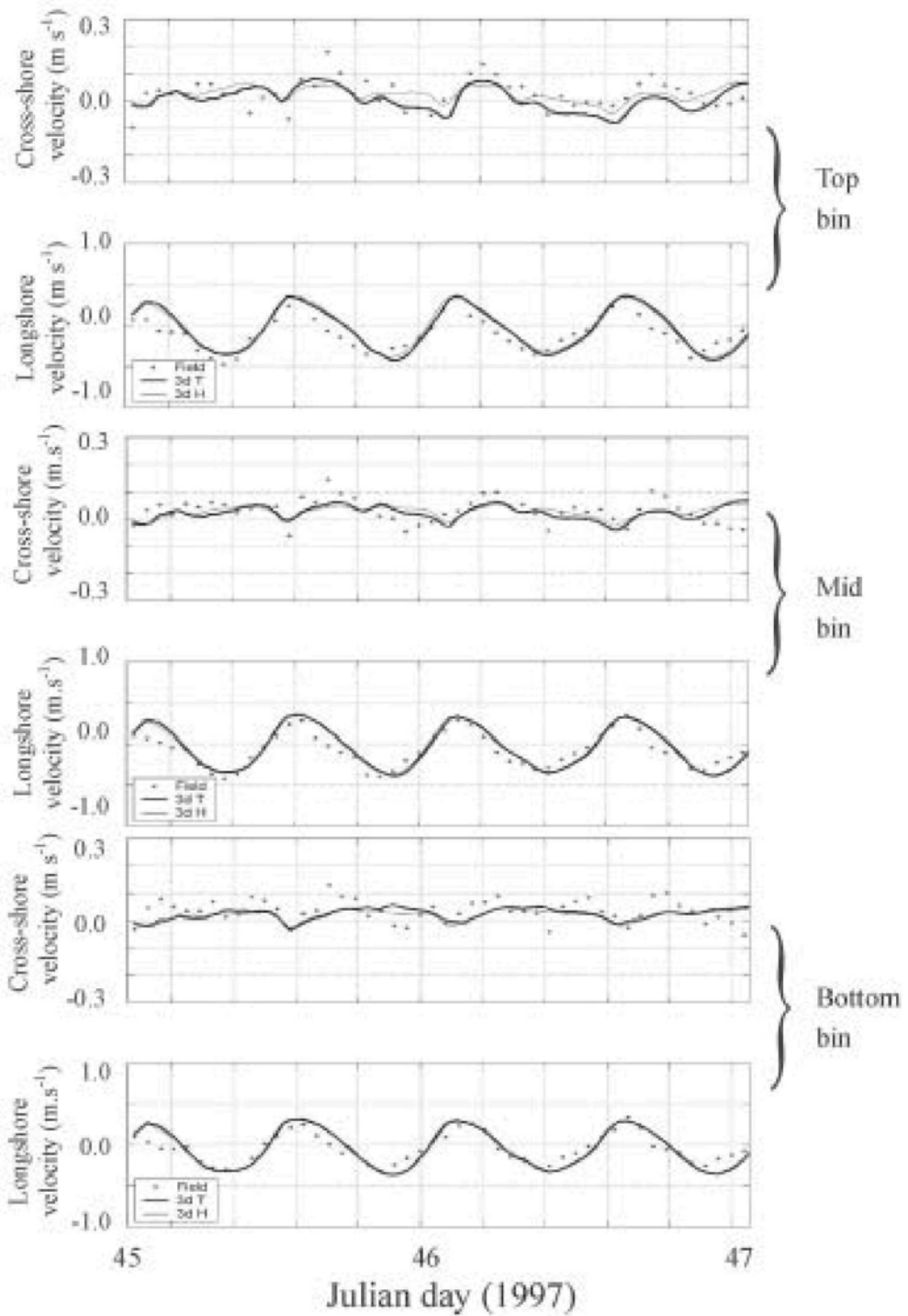


Fig. 11 Comparison of the calibrated barotropic (light solid line) and baroclinic (heavy solid line) model with measurements (dots) at site 10, for near-surface, mid-water and near-bed.

the model leads the data slightly, the model is responding to the processes driving this measured lag.

The cross-shore dynamics are also reproduced near the bed (Fig. 10). Most importantly, the magnitudes are of the right order. Particularly evident is the reproduction of the variations in asymmetry of the time series between cycles in the model, notwithstanding the sharp peak at 46.6 days near the bed that is not reproduced. At the near-surface site, the character of the time series is completely different to the bed measurements, and the model is reproducing some segments but not all. In general, the magnitudes are close but the data show more variability.

At site 10, the predicted longshore currents agree with the measurements (Fig. 11), although the asymmetry over the tidal cycles appears to be slightly more pronounced in the model. The most distinctive characteristic is the asymmetry of the time series at site 10 (not present in the measurements or model at site 9) that is reproduced by the model. Also, the in-phase synchrony of the near-bed and near-surface flows is being reproduced.

The cross-shore time series are characterised by irregular peaks, which are not well correlated with the dominant M_2 tidal oscillation or with the model.

Predicted currents from both the barotropic and baroclinic model are included in Fig. 10 and 11 as a thin and thick line respectively. The differences between the two time series are small and not significant in the longshore direction, but the differences are more marked cross-shore where the currents are smaller. With the scatter in the cross-shore measurements, no assertions are possible about which example of the model fits the data best, as both are equally close to the measurements. One conclusion to be drawn is that stratification appears to be only slightly influencing the horizontal circulation at these sites, but we continue to model the stratification both as a tracer and to ensure that the dynamics are represented as accurately as possible.

Baroclinic calibration results: isotherms

If the paucity of the field measurements including the lack of data adjacent to the coast is accounted for, the model behaves similarly to measured isotherms. Particularly strong is the association of the vertical currents in the model and the isotherm movement in the measurements. Two examples are shown in Fig. 12 and 13, which relate to conditions of strong onshore and offshore winds (Fig. 2).

In Fig. 12, the bulge and dip towards the coast is associated with the downward flows near the coast. The upward projection of the isotherm at high water + 3 h and disappearance of the bulge associates with the downward flows offshore and the upward flows near the coast. Similarly at high water + 6 h. At high water + 9 h the common trend in the data is for the upper level isotherms to diverge upward, while the deeper isotherms diverge down. This associates with a complex circulation near the coast with strong offshore and downward flow near the surface, upward flow further offshore, and up/offshore flow at depth.

Similarly in Fig. 13, many of the same trends are observed. One of the strongest agreements is seen at high water + 9 h where the coastal isotherms measured 925 m from the shore dip down sharply near the coast at the time when the model is predicting a narrow band of strong downward flows against the coast. Similarly, the dropping isotherms in the measurements between high water + 3 h and high water + 6 h are reflected by a downward flow in the model.

Similar agreement was obtained with the other two examples simulated (figures not presented here).

Calibration summary

We have examined currents at four sites, and predictions through the water column were available at the critical sites 9 and 10 in the eddy. We have also examined eddy dynamics inferred from the horizontal and vertical movement of the isotherms. There are some deviations between the model and data, the most significant being the under-prediction of the velocity phase shift between the surface and bed at site 9. However, the modelled currents and isotherm movements are behaving similar to the measurements. With its better spatial resolution than the field data, the model can be used to infer more about the eddy and its patterns of circulation.

Description of the eddy dynamics

In Fig. 14–16, the eddy is shown in plan and cross-section. The plan depicts the surface layer in the model ($K = 1$) at 0–4.5 m depth. The cross-sections are through $J = 30$ on the headland, $J = 33$ at 1.2 km north, and $J = 36$ at 2.4 km north in the northern segment of the eddy (Fig. 8A). Five examples were modelled (calm, north-east, south-east, north-west, south-west) and three are presented, i.e., calm, north-east, and south-east winds of 10 m s^{-1} . As the circulation is very complex, the dominant flow patterns are summarised with bold arrows in each panel.

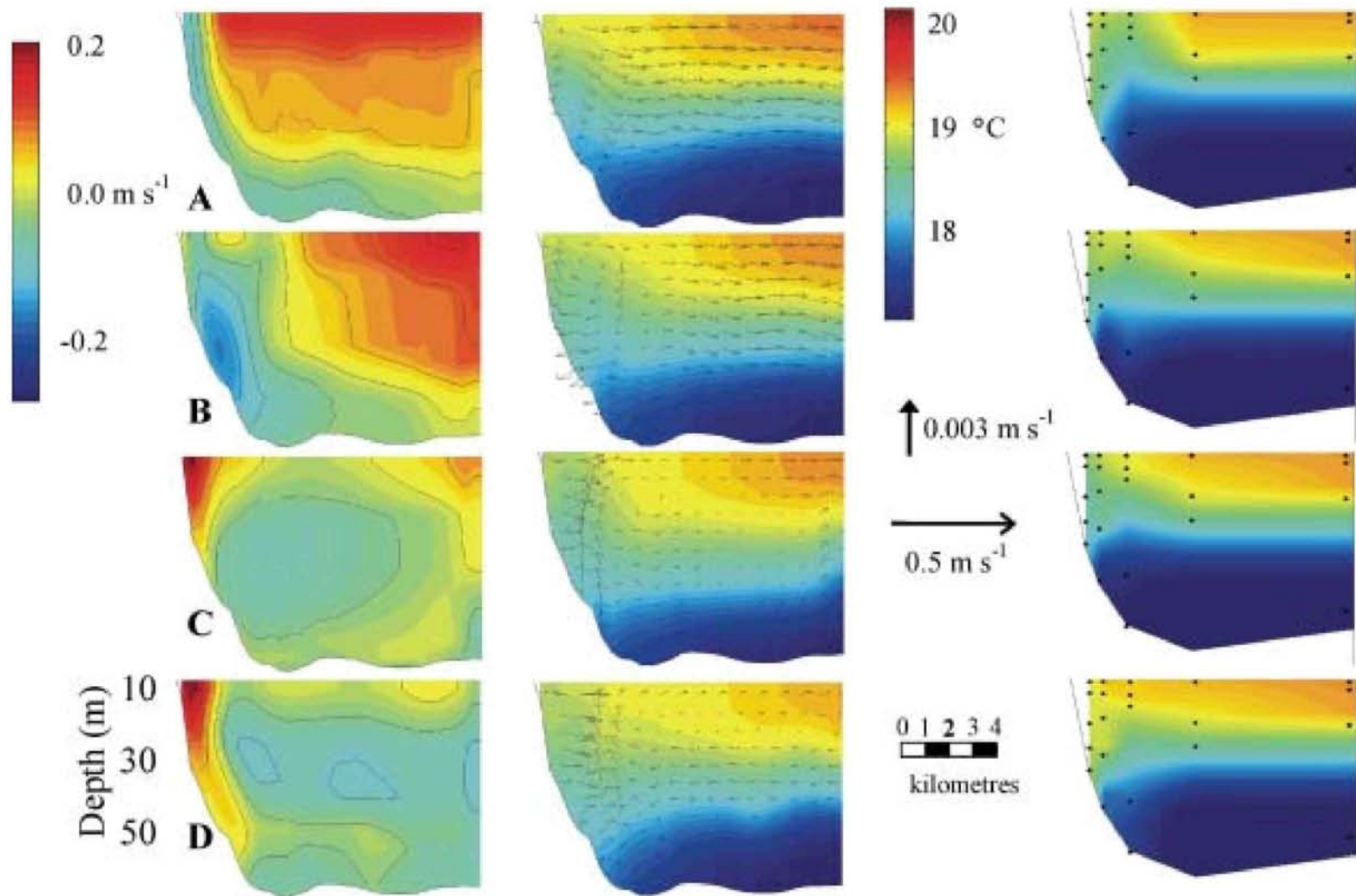


Fig. 12 Comparison of thermistor data and model for calibration period I (Julian day 40.9) for: **A**, high water; **B**, high water + 3 h; **C**, high water + 6 h (Low water); and **D**, high water + 9 h. Left column shows currents through a transect to the north of the headland ($J = 33$) from the model. Middle column shows velocities along the transect and isotherms from the model. Right column shows measured interpolated temperatures.

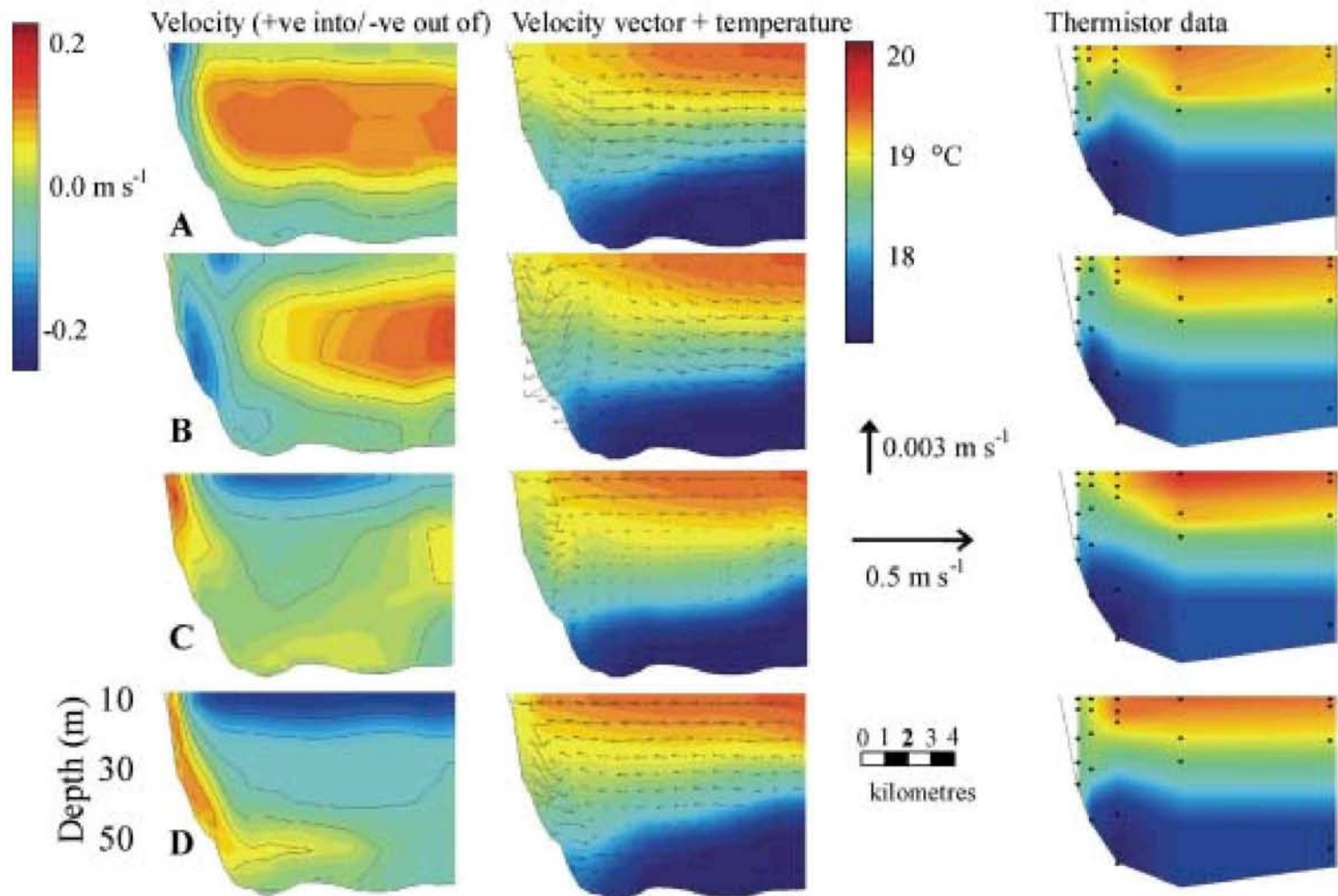


Fig. 13 Comparison of thermistor data and model for calibration period II (Julian day 43) for: **A**, high water; **B**, high water + 3 h; **C**, high water + 6 h (low water); and **D**, high water + 9 h. Left column shows currents through a transect to the north of the headland ($J = 33$) from the model. Middle column shows velocities along the transect and isotherms from the model. Right column shows measured interpolated temperatures.

Horizontal circulation

The eddy evolves in the surface layer as follows (Fig. 14, left column, $K = 1$). At high water (Fig. 14A), horizontal currents from the south side of the headland lead the free stream so that flows are fast to the north near the headland while slack offshore. North of the headland the currents bifurcate and penetrate into the headland lee. The horizontal currents continue to accelerate with the free stream at 1.5 h (Fig. 14B). The headland orientation on the south side directs flows offshore in the jet to the north. The region of jetting flow off the headland travels north and offshore and a wake forms in the lee of the headland at 3 h (Fig. 14C). Currents turn towards the shore by rotating anti-clockwise and, in the northern extremity of the eddy, the flow reverses first against the coast. The core of the eddy is well north of the headland at 4.5 h (Fig. 14D). The core then migrates south and offshore over the next 1.5 h until currents are strong against the coast and slack offshore at low tide.

Vertical circulation

During calm conditions off the headland (Fig. 14, $J = 30$), the strongest currents are adjacent to the headland as suspected from the thermistor strings that showed maximum temperature fluctuations at site 10 nearest the coast (Fig. 5). At high tide, the offshore orientation of the jetting flow leads to upwelling against the coast, which rotates and downwells further offshore (Fig. 14A, B at $J = 30$). This trend for upwelling near the coast continues until low tide (Fig. 14E, $J = 30$) when a strong downward jet occurs along the offshore edge of the return flow along the headland. This creates a vertical eddy in the upper half of the water column.

At $J = 33$ in calm conditions (Fig. 14), the patterns are significantly different. Here, a narrow jet of upwelling very near the seabed at high water (Fig. 14A, $J = 33$) is replaced by downwelling offshore and mostly shoreward flow, with a strong landward flow along the seabed at depth (Fig. 14B, $J = 33$). This seabed inflow is subsequently replaced by an offshore current at the bed at low tide (6 h) and a complex pattern of rotation higher in the water column. Around 1.5 and 3 h at $J = 33$, a strong downwelling in the centre of the jetting region meets the shoreward flow along the seabed at mid depth, and the currents turn upward against the coast (Fig. 14E, $J = 33$). The observed isotherm observations are seen to behave similarly.

Further north at $J = 36$, circulation is shoreward and upward from high water until 4.5 h (Fig. 14A–D,

$J = 36$). The vertical thickness of the zone of strong currents grows through time. It is initially only close to the bed at high water, but becomes strong and shoreward across the full model domain at 1.5 to 4.5 h. At low tide however, the pattern is complex with the flow heading shoreward in the offshore region, while the currents near the headland are oppositely directed (Fig. 14E, $J = 36$). This leads to a convergence, generally directed down along the seabed.

Wind effects

The addition of north-east (onshore) wind into the simulation alters the patterns observed during the tide-only (calm conditions) example. First, the eddy is weaker (compare Fig. 14D and 15D, $K = 1$) and the eddy is compressed against the coast for north-east wind. On the contrary, the width of the return flow region greatly expands and the core of the eddy moves offshore and to the north under south-west winds (figure not shown), relative to the calm condition. Along the headland transect ($J = 30$), strong upwelling evident at depth converges with an offshore flow around the 1/3 depth position, so that surface penetration of the isotherms is not likely to be strong (Fig. 15A–D, $J = 30$).

In the south-easterly example, the upwelling induced by the eddy has been totally over-ridden, so that the currents in the upper two thirds of the water column near the coast are totally downwelling oriented (Fig. 16A–E, $J = 30$). An inshore and upward flow still occurs near the seabed at 1.5 h, and this meets the downwelling at c. $\frac{2}{3}$ of the depth (Fig. 16B, $J = 30$). The patterns at low water are strongly downwelling but remain complex at depth (Fig. 16E, $J = 30$). The other transects show predominantly onshore movement, particularly at the surface (Fig. 16A–E, $J = 33$ and 36).

General isotherm patterns and surface manifestations

Isotherms from the baroclinic model at high water plus 4.5 h during calm (tide-only) and north-east, south-east, south-west, and north-west winds are shown in Fig. 17. This is when the eddy is strongest under all wind conditions. Also presented are the surface temperatures (indicating upwelling evidenced by penetration to the surface of underlying cooler water).

One of the interesting results is the advection of cold water from the south of the headland during the north-west wind (Fig. 17E, surface) and the disappearance of the eddy during a south-east wind

Fig. 14 Calm wind example showing eddy dynamics from the baroclinic model at: **A**, high water; **B**, high water + 1.5 h; **C**, high water + 3 h; **D**, high water + 4.5 h; and **E**, high water + 6 h (near low tide). Velocity vectors in the surface layer ($K = 1$ at 0–4.5 m depth) are in the left column, and currents along cross-sections through $J = 30, 33,$ and 36 are in subsequent columns. Bold arrows show the general directions of flow.

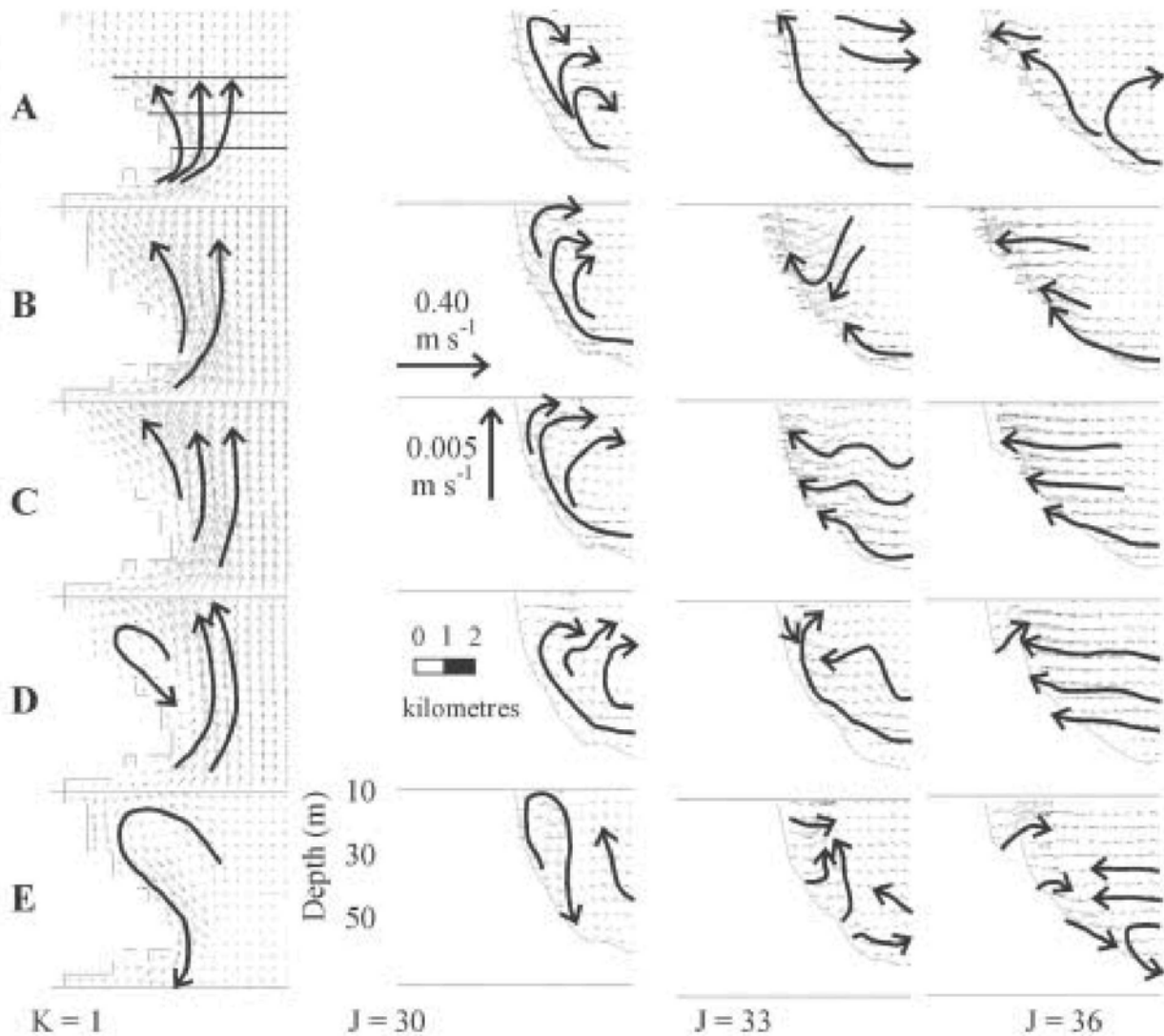


Fig. 15 North-east wind example showing eddy dynamics from the baroclinic model at: **A**, high water; **B**, high water + 1.5; **C**, high water + 3 h; **D**, high water + 4.5 h; and **E** high water + 6 h (near low tide). Velocity vectors in the surface layer ($K = 1$ at 0–4.5 m depth) are in the left column, and currents along cross-sections through $J = 30, 33,$ and 36 are in subsequent columns. Bold arrows show the general directions of flow.

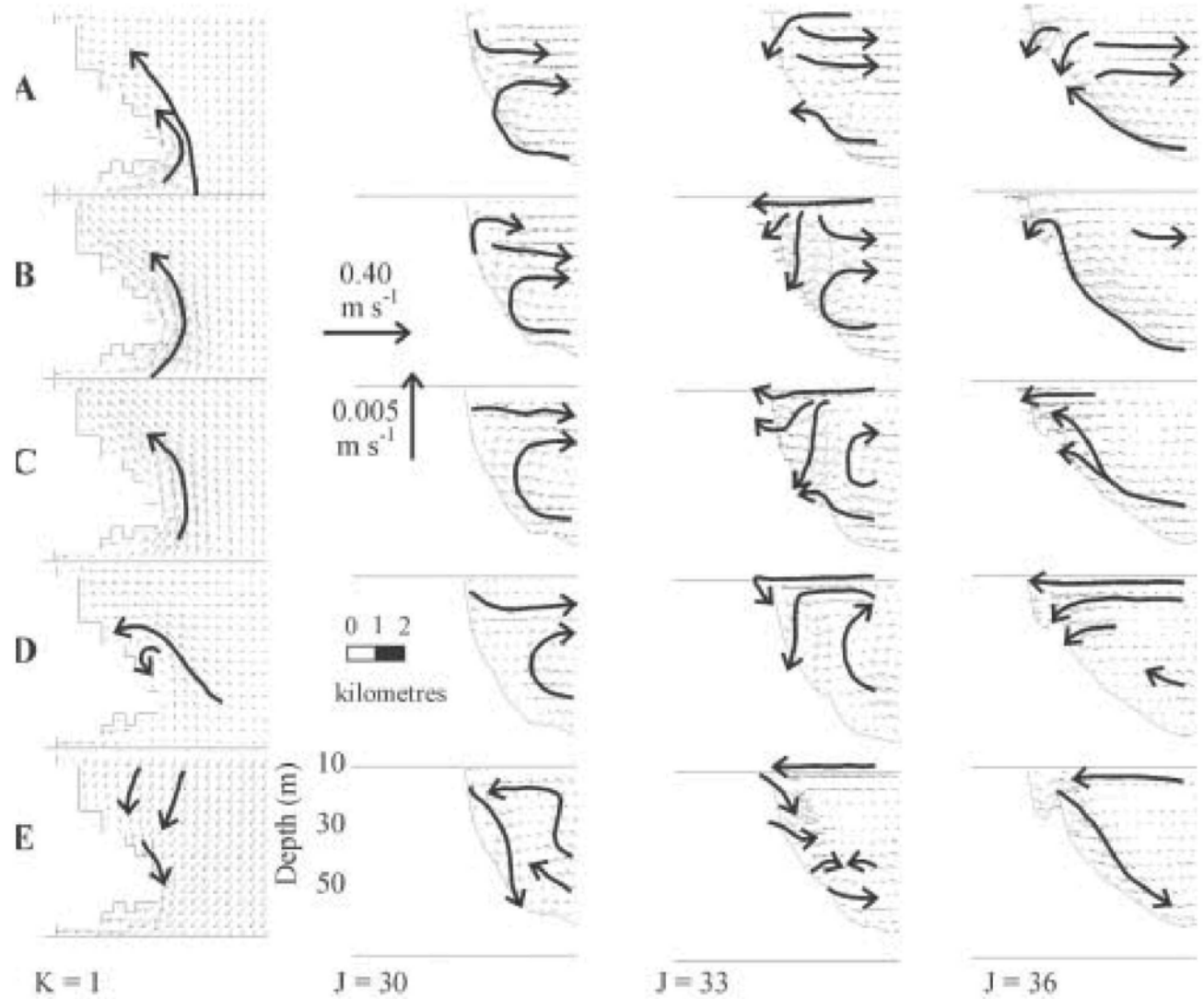
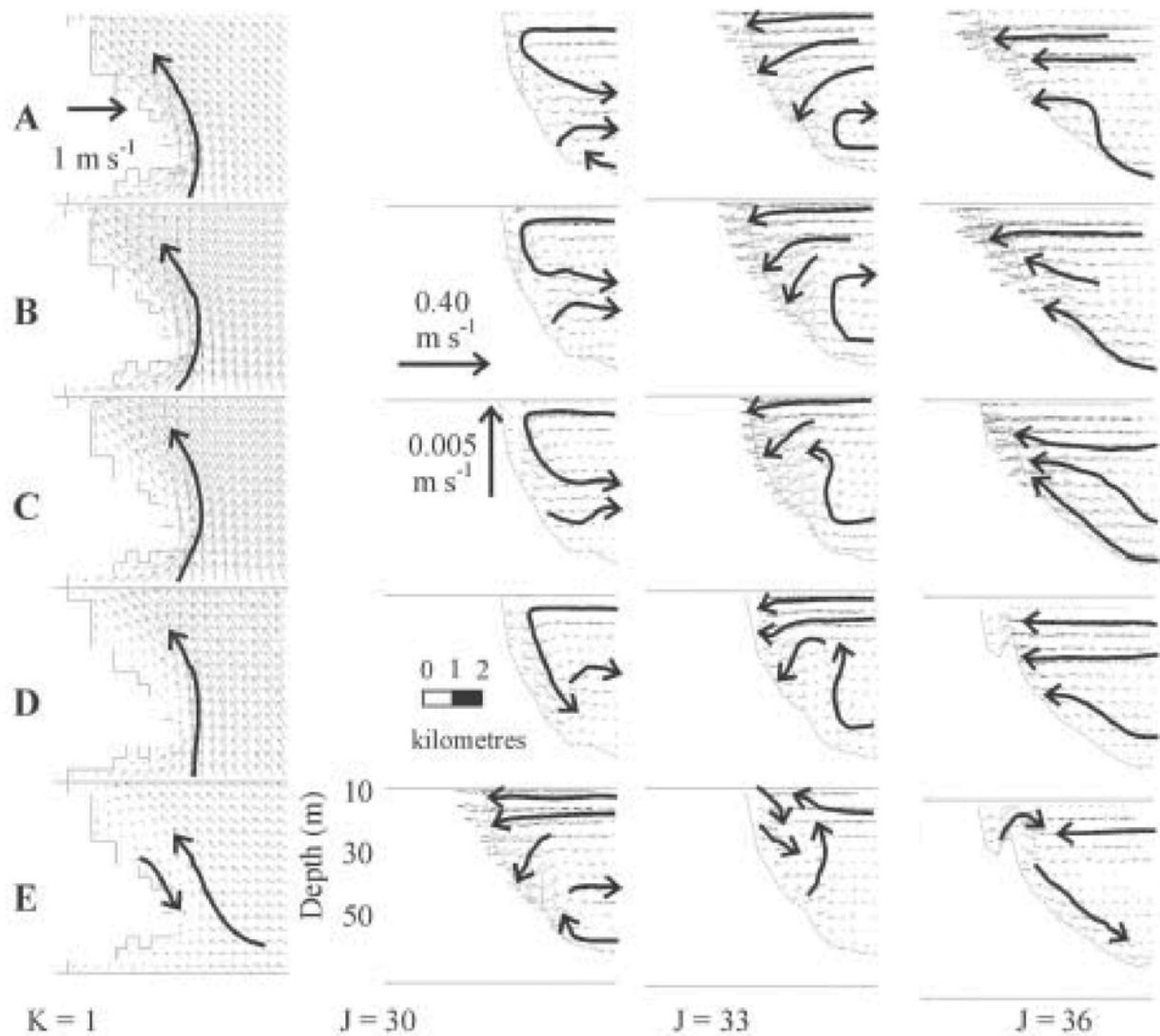
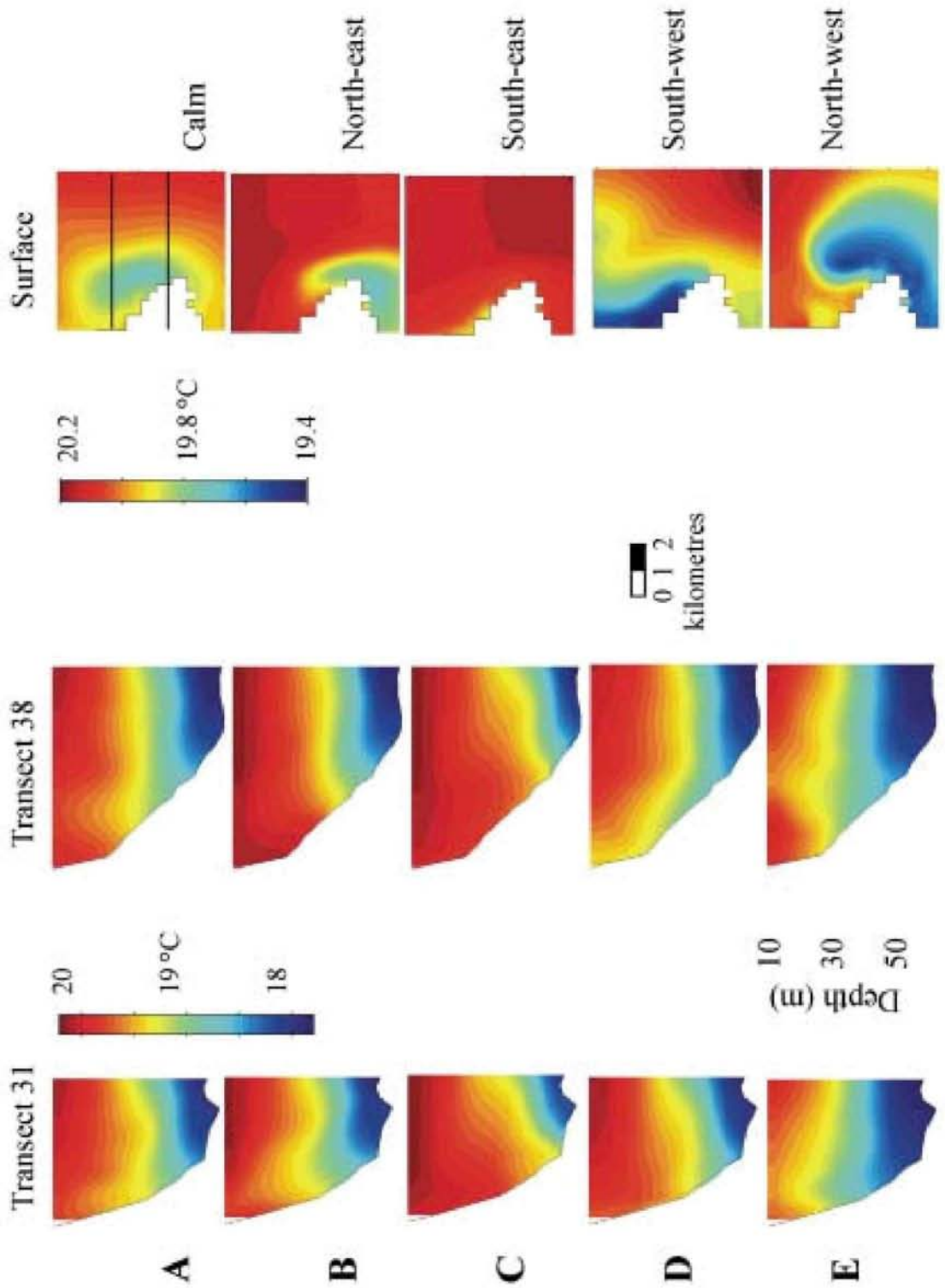


Fig. 16 South-east wind example showing eddy dynamics from the baroclinic model at: **A**, high water; **B**, high water + 1.5 h; **C**, high water + 3 h; **D**, high water + 4.5 h; and **E**, high water + 6 h (near low tide). Velocity vectors in the surface layer ($K = 1$ at 0–4.5 m depth) are in the left column, and currents along cross-sections through $J = 30$, 33, and 36 are in subsequent columns. Bold arrows show the general directions of flow.





◀ **Fig. 17** Temperatures at 4.5 h after high tide from the baroclinic model under: **A**, calm; **B**, north-east; **C**, south-east; **D**, south-west; and **E**, north-west winds of 10 m s^{-1} , through two cross-sections ($J = 31$ and 38) (left columns) and at the surface (right column).

(Fig. 17C, surface). The eddy is clearly evident in calm conditions (Fig. 17A, surface). Each of these modelled results is in accordance with the field data (e.g., Fig. 8). For both north-west and south-west winds, there is a resemblance between the model data (Fig. 17D,E, surface) and the equivalent field data (Fig. 8C,A).

In cross-section, the isotherms are strongly influenced by wind, with upwelling being greatest during the south-west wind (Fig. 17D, $J = 31$, $J = 38$) and smallest during a south-east wind (Fig. 17C). The calm and north-west examples (Fig. 17A,E) both show the tendency for maximum upwelling to occur away from the coast in $J = 38$, with a strong upward bulging of the isotherms being particularly evident during the north-westerly wind (Fig. 17E).

DISCUSSION

Horizontally, the eddy stretches c. 5 km along the headland and appears to be c. 1.5–2.0 km wide in the numerical model, lasting a short time of c. 2 h and moving in space. This occurs throughout most cycles, unless the winds are strong. Unpublished measurements with a ship-borne ADP to the north of the headland (Hume 1997b) confirmed the presence and size of the eddy (not reproduced here). Similarly, seabed observations also showed the signature of the eddy in the sediment texture and bedform characteristics about the headland (Hume et al. 1997a, 2000).

The eddy has the features of a phase eddy (Black & Gay 1987); it develops in the wake after peak flow and the return flow strengthens while the free stream is still decelerating, and is transient. An examination of the model terms in the horizontal momentum balance for the calm condition at the time of eddy formation showed that, excluding the driving pressure gradients, advection is the dominant term at c. $1 \times 10^{-5} \text{ m s}^{-2}$, in accordance with previous findings of Black & Gay (1987) and Black (1989). The Coriolis force is c. $2 \times 10^{-7} \text{ m s}^{-2}$, whereas the horizontal eddy viscosity is c. $1 \times 10^{-6} \text{ m s}^{-2}$. Of course, the largest term is the sea surface gradient, which is c. $2 \times 10^{-5} \text{ m s}^{-2}$ in the vicinity of the eddy.

Thus, the dominant terms in the eddy are inertia (advective momentum) and sea surface gradient. The advection maintains the straight-line path of the water flow and is particularly strong off the headland. This allows the wake to form in the sheltered waters in the lee of the headland. The change in sea gradient after peak ebb tidal flow then accelerates the wake as a return flow, while the free stream continues to decelerate, and so the eddy appears.

Factors like horizontal eddy viscosity and Coriolis force play a modifying role. Indeed, the Coriolis term assists the rotation of the currents to the left in the lee of the headland, thereby supporting the anticlockwise rotation in the eddy. However, a stronger clockwise eddy forms on the south side of the headland, which is opposed by the Coriolis force, because of the greater depth on steeper topography to the south, and so topography has a stronger role.

The measured isotherms and currents and the numerical modelling all indicate eddy hydrodynamics through the water column that are very complex, particularly close to the coast. For example, the current is only upward in the core of the eddy at limited stages of the tide. The patterns of circulation are actually far more complex as the eddy is often partitioned vertically into three layers. Currents can be simultaneously upward or downward in different layers at any one time and the eddy is transient. Although the hydrodynamic model calibration indicates that the results appear similar in the barotropic and baroclinic models, the patterns of flow were found to be significantly more complex in the stratified model (figures not shown), indicating that stratification changes eddy character.

Some of our expectations in relation to the previously-published dynamics of eddies have been proven, such as the transfer of deep water to the surface. However, even this process is not always evident as the upwelling is overcome during onshore wind events. The eddy is strictly never free of the headland. Unlike larger ocean eddies, its dissipation is not on a time-scale that relates to internal or bed friction, or the conservation of vorticity. The eddy is phase locked with the tidal period. It evolves with the changing large-scale tidal pressure gradient (the eddy forms during each ebb cycle) and dissipates at the end of the cycle. Thus, there is very little free vorticity as such. The phase eddy is more like two independent streams of adjacent water; one near the headland travels along the coast towards the headland, while the other stream offshore travels oppositely. The loop is completed by continuity and

shear infusion of momentum between the streams. The headland stream is accelerating while the offshore stream is still decelerating, both in response to the changed sign of the large-scale tidal pressure gradient. Thus, although a rotation indicates the presence of vorticity, by definition the feature is not a vortex, as defined for long-lived eddies responding to the laws of conservation of angular momentum in the presence of friction.

As inferred initially from the isotherms, most of the vertical circulation occurs adjacent to the coast. Also, the vertical circulation is different between the jetting current of the headland and the return flow. Currents can be initially directed down and offshore near the coast, but simple patterns are often replaced by complex circulation. Recurring patterns were identified. Most common is the upward bulging of the isotherms at site 9 around high tide to be replaced by an upwelling shoreward of site 10 at peak ebb flow (3 h later) and finally by downwelling at peak flood flow (9 h). When downwelling near the coast at 6–9 h, the currents are strongly upwelling offshore near site 9. At peak ebb (3 h) when the eddy first forms, the opposite occurs with downwelling near site 9, while upwelling occurs near the coast. The trend for horizontal circulation at the surface to be 2 h out of phase with the near-bed currents at site 9 is also a common event.

The circulation is strongly influenced by seabed morphology, density structure, and weather, potentially making some characteristics of each headland eddy unique in its own environment. The study has shown that the eddy on Cape Rodney is a phase eddy with complex characteristics affected by morphology, tidal current magnitude, wind, and stratification. Internal circulation within the eddy is strongest near the bed and against the coast and vertical eddies readily form in parts of the water column, but these eddies rarely penetrate through the full depth. The dynamics near the surface and near the bed are significantly different and the structure of the eddy is often partitioned vertically into three layers: surface, mid-depth, and near bed. Eddy structure significantly varies in space (in cross-sections along the headland) and in time (between successive tidal cycles).

ACKNOWLEDGMENTS

We thank Dr Rob Bell of NIWA for his assistance with the tidal analyses and mean water level adjustments needed to create the model boundaries. The project was

funded by the Foundation for Research, Science and Technology ("Nearshore offshore exchanges", contract no. C01511).

REFERENCES

- Beer, T. 1997: Environmental oceanography. 2nd ed. Boca Raton, Florida, CRC Press Inc. 367 p.
- Black, K. P. 1987: A numerical sediment transport model for application to natural estuaries, harbours and rivers. *In*: Noye, J. ed. Numerical modelling applications to marine systems. North Holland, Elsevier. Pp. 77–105.
- Black, K. P. 1989: Numerical simulation of steady and unsteady meso-scale eddies. Proceedings of the 9th Australasian Conference on Coastal and Ocean Engineering, Adelaide. Pp. 204–208.
- Black, K. P. 1994: Developments in our knowledge of dispersal on the Great Barrier Reef. *In*: Sammarco, P. L.; Heron, M. L. ed. The biophysics of marine larval dispersal. Coastal and Estuarine Studies, American Geophysical Union. Pp. 159–192.
- Black, K. P. 1995: The hydrodynamic model 3DD and support software. Occasional Report 19, Department of Earth Sciences, University of Waikato. 53 p.
- Black, K. P.; Healy, T. R. 1982: Sediment transport investigations in a New Zealand tidal inlet. Proceedings of the 18th International Coastal Engineering Conference, Cape Town, American Society of Civil Engineers. Pp. 2436–2457.
- Black, K. P.; Gay, S. L. 1987: Eddy formation in unsteady flows. *Journal of Geophysical Research* 92: 9514–9522.
- Black, K. P.; Gay, S. L. 1991: Reef-scale numerical hydrodynamic modelling developed to investigate crown-of-thorns starfish outbreaks. *In*: Bradbury, R. ed. Acanthaster and the coral reef: a theoretical perspective. Springer-Verlag. Pp. 120–150.
- Black, K. P.; Hatton, D.; Rosenberg, M. 1993: Locally and externally-driven dynamics of a large semi-enclosed bay in southern Australia. *Journal of Coastal Research* 9(2): 509–538.
- Black, K. P.; Bell, R. G.; Oldman, J. W.; Carter, G. S.; Hume, T. M. 2000: Features of 3-dimensional barotropic and baroclinic circulation in the Hauraki Gulf, New Zealand. *New Zealand Journal of Marine and Freshwater Research* 34: 1–28.
- Deleersnijder, E.; Norro A.; Wolanski, E. 1992: A three-dimensional model of the water circulation around an island in shallow water. *Continental Shelf Research* 12(7/8): 891–906.

- Denniss, T.; Middleton J. H. 1994: Effects of viscosity and bottom friction on recirculating flows. *Journal of Geophysical Research* 99(C5): 10,183–10,192.
- Denniss, T.; Middleton J. H.; Manasseh, R. 1995: Recirculation in the lee of complicated headlands: a case study of Bass Point. *Journal of Geophysical Research* 100: 16,087–16,101.
- Falconer, R. A.; Mardapitta-Hadjipandeli, L. 1987: Bathymetric and shear stress effects on an island's wake: computational model study. *Coastal Engineering* 11: 57–86.
- Falconer, R. A.; Wolanski, E.; Mardapitta-Hadjipandeli, L. 1984: Numerical simulation of secondary circulation in the lee of headlands. Proceedings of the 19th International Coastal Engineering Conference, American Society of Civil Engineers. Pp. 2414–2433.
- Falconer, R. A.; Wolanski, E.; Mardapitta-Hadjipandeli, L. 1986: Modelling tidal circulation in an island's wake. *Journal of Waterway Port Coastal and Ocean Engineering* 112: 234–254.
- Freeland, H. J. 1990: The flow of a coastal current past a blunt headland. *Atmosphere-Ocean* 28: 288–302.
- Furukawa, K.; Wolanski, E. 1998: Shallow water frictional effects in island wakes. *Estuarine, Coastal, and Shelf Science* 31: 231–253.
- Galloway, D.; Wolanski, E.; King, B. 1996: Modelling eddy formation in coastal waters: a comparison between model capabilities. In: Spaulding, M. L.; Cheng, R. T. ed. *Estuarine and coastal modelling*. Proceedings of the 4th International Conference, American Society of Civil Engineers. Pp. 13–24.
- Geyer, W. R.; Signell, R. P. 1991: Measurements and modelling of the spatial structure of non-linear tidal flow around a headland. In: Parker, B. P. ed. *Tidal hydrodynamics*. John Wiley & Sons. Pp. 403–418.
- Hume, T. M.; Black, K. P.; Oldman, J. W.; Vennell, R. 1997a: Signatures of wave and current forcing on the seabed about a large coastal headland. Pacific Coasts and Ports '97, Proceedings of the 13th Australasian Coastal & Ocean Engineering Conference, Christchurch, New Zealand. Vol. 1. Centre for Advanced Engineering, University of Canterbury. Pp. 319–324.
- Hume, T. M.; Vennell, R.; Black, K. P. 1997b: Sounding out the currents. *NIWA Water and Atmosphere* 5(2): 19–21.
- Hume, T. M.; Oldman, J. W.; Black, K. P. 2000: Sediment facies and pathways of sand transport about a large deep water headland, Cape Rodney, New Zealand. *New Zealand Journal of Marine and Freshwater Research* 34: 695–717.
- Klinck, J. M. 1996: Circulation near submarine canyons: a modelling study. *Journal of Geophysical Research* 101(C1): 1211–1223.
- Lamb, K. G. 1994: Numerical simulations of stratified inviscid flow over a smooth obstacle. *Journal of Fluid Mechanics* 260: 1–22.
- Lee, H.-J.; Chao, S.-Y.; Fan, K.-L. 1999a: Flood-ebb disparity of tidally induced recirculation eddies in a semi-enclosed basin: Nan Wan Bay. *Continental Shelf Research* 19(7): 871–890.
- Lee, H.-J.; Chao, S.-Y.; Fan, K.-L.; T.Y. Kuo, 1999b: Tide-induced eddies and upwelling in a semi-enclosed basin: Nan Wan. *Estuarine, Coastal, and Shelf Science* 49: 775–787.
- Leendertse, J. J.; Liu, S.-K. 1975: Modelling of three dimensional flows in estuaries. 2nd Annual Symposium on Modelling Techniques, Waterways Harbours and Coastal Engineering, American Society of Civil Engineers. Pp. 625–642.
- Maddock, L.; Pingree, R. D. 1978: Numerical simulations of Portland Bill tidal eddies. *Estuarine and Coastal Marine Science* 6: 353–363.
- Middleton, J. F.; Black, K. P. 1994: The low frequency circulation in and around Bass Strait: a numerical study. *Continental Shelf Research* 14(13/14): 1495–1521.
- Middleton, J. H.; Griffin, D. A.; Moore, A. M. 1993: Oceanic circulation and turbulence in the coastal zone. *Continental Shelf Research* 13(2/3): 143–168.
- Pattiaratchi, C.; James, A.; Collins, M. 1987: Island wakes: a comparison between remotely sensed data and laboratory experiments. *Journal of Geophysical Research* 92(C1): 783–794.
- Perenne, N.; Verron, J.; Renouard, D.; Boyer, D. L.; Zhang, X. 1997: Rectified barotropic flow over a marine canyon. *Journal of Physical Oceanography* 27: 1868–1893.
- Perrels, P. A. J.; Karelse, M. 1982: A two-dimensional laterally averaged model for salt intrusion in estuaries. *Delft Hydraulics Laboratory Report No. 262*.
- Pingree, R. D.; Maddock, L. 1979: The tidal physics of headland flows and offshore tidal bank formation. *Marine Geology* 32: 269–289.
- Signell, R. P.; Geyer, W. R. 1991: Transient eddy formation around headlands. *Journal of Geophysical Research* 96(C2): 2561–2575.
- Wolanski, E.; Imberger, J.; Heron, M. L. 1984: Island wakes in shallow coastal waters. *Journal of Geophysical Research* 89(C6): 10,553–10,569.
- Wolanski, E.; Asaeda T.; Tanaka, A.; Deleersnijder, E. 1996: 3-Dimensional island wakes in the field, laboratory experiments and numerical models. *Continental Shelf Research* 16(11): 1437–1452.

- Wu, J. 1982: Wind stress coefficients over sea surface from sea breeze to hurricane. *Journal Geophysical Research* 87: 9704–9706.
- Young, I. R.; Black, K. P.; Heron, M. L. 1994: Circulation in the ribbon reef region of the Great Barrier Reef. *Continental Shelf Research* 14(2/3): 117–142.